Monthly Notices
of the
ROYAL ASTRONOMICAL SOCIETY

MNRAS **524,** 1826–1854 (2023) https://doi.org/10.1093/mnras/stad1891
Advance Access publication 2023 June 24

Time-series photometry and multiwavelength characterization of the young stellar cluster Mon R2

Santiago Orcajo ,[1,2]★ Lucas A. Cieza[3] and Roberto Gamen [1,2]

[1]*Facultad de Ciencias Astronómicas y Geofísicas, Universidad Nacional de La Plata, Paseo del Bosque S/N, B1900 La Plata, Argentina*
[2]*Instituto de Astrofísica de La Plata, CCT La Plata, CONICET–UNLP, B1900 La Plata, Argentina*
[3]*Núcleo de Astronomía, Facultad de Ingeniería y Ciencias, Universidad Diego Portales, Av Ejército 441, 8320000 Santiago, Chile*

Accepted 2023 June 11. Received 2023 June 9; in original form 2021 August 26

ABSTRACT

Using the Las Cumbres Observatory Global Telescope Network (LCOGT), we have obtained multi-epoch photometry of the young cluster Mon R2. We have monitored over 6000 sources with *i*-band between 13 and 23 mag within a 26 × 26 arcmin^2 field of view. For each star, we collected ∼1500 photometric points covering a temporal window of 23 d. Based on these data, we have measured rotation-modulated of 136 stars and identified around 90 additional variables, including 14 eclipsing binary candidates. Moreover, we found 298 other variables with photometric high-scatter. In addition, we have obtained *r*-band and Hα narrow-band photometry of the cluster with LCOGT and low-resolution optical spectroscopy of 229 stars with GMOS-Gemini. We used the *Gaia* data from the periodic stars and objects with Hα or IR-excesses, which are mostly low-mass pre-main sequence stars ($<$1 M$_\odot$) in the cluster to estimate the distance (825 ± 51 pc) and the mean proper motions ($\mu_\alpha cos(\delta) = -2.75$ mas yr^{-1} and $\mu_\delta = 1.15$ mas yr^{-1}) of its members. This allows us to use the *Gaia* data to identify additional Mon R2 member candidates. We also used Pan-STARRS photometry from our LCOGT sources to construct a more precise H-R diagram, from which we estimate the mean age of the cluster and identify other possible members including eleven spectroscopy brown dwarf with M7 to M9 GMOS spectral types. Finally, we combined our membership lists with *Spitzer* infrared photometry to investigate the incidence of stars with discs and the effect these have on stellar rotation.

Key words: brown dwarfs – stars: fundamental parameters – stars: low-mass – stars: rotation – stars: variables: general – open clusters and associations: individual: Mon R2.

1 INTRODUCTION

Open clusters (OCs) are essential targets for the study of galactic structure and composition, as well as of star formation in a galaxy, including the Milky Way (see e.g. Janes & Adler 1982; Molina Lera, Baume & Gamen 2019; Zhong et al. 2020). The members of a young OC are usually assumed to have the same origin, age, and composition, although there may be some substructures of star formation within a given cluster (Lada & Lada 2003). In our nearby neighbourhood ($<$1 kpc), there are at least 655 such OCs (Sim et al. 2019).

The young OCs contain PMS stars, molecular gas, and H II regions. The dust associated with the molecular gas in young OCs interferes with the estimates of stellar distance, age, and mass. However, the combination of data sets from observatories such as *Spitzer*, *Gaia*, and Pan-STARRS provide us with a more precise and in-depth view, which allows to obtain these main stellar parameters with greater precision (e.g. Castro-Ginard et al. 2020; Fabricius et al. 2021). In turn, a more complete census of the stellar members permits to better define the structure and age of a young OC and provides observational constrains to test theories of star formation and stellar structure (e.g. Shu, Adams & Lizano 1987; Lada & Lada 2003).

In addition to age and mass, angular momentum is one of the fundamental parameters in stellar astrophysics (Rebull, Wolff & Strom 2004; Bouvier et al. 2014). Several studies have shown that, during the PMS stage, stars drain angular momentum through their circumstellar discs (e.g. Rebull 2001; Irwin et al. 2008; Venuti et al. 2017; Orcajo et al. 2019; Rebull et al. 2020). Therefore, measuring the rotation period in OCs of stars with and without a disc is key to study the evolution of angular momentum as a function of age and stellar mass. Currently, such studies can be performed through the combination of photometric rotation periods and infrared (IR) observations (used for disc identification).

In order to contribute to the understanding of OCs in our Solar neighbourhood, we have obtained time-series photometry and conducted a multiwavelength characterization of the stellar population in the OC Mon R2. The paper has a broad scope and several main goals, including identifying new stellar and substellar members, refining the distance, age, and proper motion of the cluster, identifying stars with circumstellar discs, and investigating their effect on stellar rotation. In addition to this main goals, we use the time-series photometry to identify eclipsing binaries and several types of non-periodic variables in the field.

The Mon R2 cluster is composed of a prominent reflection nebulae, dark nebulae, molecular outflows, and H II regions (Carpenter & Hodapp 2008) and located in the third quadrant of the Galaxy at an estimated distance of 830 ± 50 pc and with an estimated age of 1–10 Myr (Herbst & Racine 1976; Carpenter et al. 1997). The structure

★ E-mail: santi@fcaglp.unlp.edu.ar

and composition from this complex region have been studied in the X-ray, IR, and radio regimes (e.g. Lombardi, Alves & Lada 2011; Rayner et al. 2017; Sokol et al. 2019). B-type stars illuminate the H II regions and the IR shell at the centre of the OC (Kohno, Koyama & Hamaguchi 2001). The dense molecular regions show arc-like structures surrounding the H II regions composed of three clumps, and an IR cluster is located at the far-side of OC (Choi et al. 2000). Carpenter & Hodapp (2008) described this cluster in detail, concluding that Mon R2 is very young and complex star formation site.

Also, Carpenter et al. (1997) studied the central region photometrically and 34 stars spectroscopically. They obtained a lower limit of ∼475 cluster members with a limiting *K*-band magnitude of 17.4 mag. Andersen et al. (2006) found that 27 ± 9 per cent of the stars with estimated masses between 0.1 and 1.0 $M_\odot$ have a near-IR (NIR) excess indicative of a protoplanetary disc. However, the low-mass (sub)stellar population in Mon R2 still remains to be studied and characterized in detail.

Here, we present a multitechnique and multiwavelength characterization of Mon R2. First, we used Las Cumbres Observatory Global Telescope Network (LCOGT) to obtain time-series photometry to identify periodic and variables sources in *I*-band. The *I*-band was chosen as a compromise between the S/N and the amplitude of the expected variations due to stellar spots and to minimize the contribution from either accretion or disc emission to the measured stellar flux. In particular the red colours of M-type stars imply that the stars are significantly brighter in the *i*-band with respect to the *r*-band. In low-mass stars, the rotation-modulated variability is due to cool (stellar activity) and hot (accretion-shocked) spots. The cool spots can cover up to the ∼40 per cent of the stellar surface and usually dominate the periodic variability (Herbst et al. 1994; Rebull 2001). Additional photometry was obtained in *R*-band and Hα narrow-band to select sources with Hα emission. The (*R* −Hα) colour allows us to identify PMS stars and discard non-member stars, i.e. giant field stars. The (*R* −Hα) colour of many PMS stars, in particular accreting classical T Tauri stars (CTTSs), is larger than the colour of a main-sequence (MS) stars of the same spectral type. The Hα emission in non-accreting weak-lined T Tauri stars is weak (from chromospheric activity) and typically not detectable through narrow-band photometry. The recombination Hα line is a power full accretion indicator because it traces the ionized hydrogen produced by the UV radiation, which is caused by the magnetospheric accretion shock in young stellar objects (YSOs; Rigliaco et al. 2012). Furthermore, the giant stars have smaller (*R* −Hα) colours than MS stars of the same *R* − *I* colours for spectral types later than ∼K3. So, it is possible to discriminate between background giants and PMS stars with a (*R* −Hα) versus (*R* − *I*) colour–colour diagram (Lamm et al. 2004). Furthermore, since the Hα line in CTTSs is mostly due to disc accretion, the (*R* −Hα) colour is also a useful disc indicator. On the other hand, observational works (i.e. Fedele et al. 2010) found that the fraction of stars with mass accretion decreases fast with time, going from ∼60 per cent at 1.5–2 Myr down to ∼2 per cent at 10 Myr, this fraction is systematically lower than the fraction of stars showing near-to-mid-IR excess. So, the NIR *Spitzer* data are typically a more a robust disc indicator than the Hα photometry; however, we find that some of our sources lack *Spitzer* colours but do have (*R* −Hα) colour data.

Then, we studied the LCOGT sources with astrometric data (ϖ, $\mu_\alpha \cos\delta$ and μ_δ) from *Gaia* Data Release 2 (GDR2) and Early Gaia Data Release 3 (EGDR3) to define specific *Gaia* membership criteria for the cluster. Also, using mid-IR photometry, we identified objects with and without IR excess from a disc. The rotation periods of Mon R2 members were correlated with disc indicators to investigate disc regulation. We also used the Pan-STARRS 1 (PS1) Data Release 1 and 2 (DR1 and DR2, respectively) photometric data to construct the H-R diagram of the OC and calculate its average age with isochrones from theoretical models. Finally, we used the low-resolution spectroscopy with the GMOS instrument on Gemini-South Observatory (GS) to classify low-mass stars and brown dwarfs (BDs).

This paper is organized as follow. In Section 2, we describe our own observations: the photometry and spectroscopy data from Las Cumbres Observatory and Gemini South Observatory, respectively. We also describe the different public data sets used for our analysis. In Section 3.1, we present the analysis of the LCOGT photometry and the GMOS spectroscopy data, with the study of light curves of the variable sources and the spectral characterization of the targets. Then, we combine the data sets to identify new (sub)members and characterize the distance, extinction, age, disc frequency, and rotation period distribution of the cluster population. Finally, in Section 4, we present a summary of our results and main conclusions.

2 OBSERVATIONS AND PUBLIC DATA SETS

2.1 Observations

2.1.1 Photometry with LCOGT

LCOGT has 23 telescopes in seven sites around the world working together, allowing to monitor a given field during several weeks or months with an almost continuous time coverage. We used the SCICAM-SINISTRO instrument at the 1.0-m telescopes, which consist of a $4K \times 4K$ CCD camera and provides a field of view (FOV) of about 26.5 × 26.5 arcmin^2, with a scale of 0.389 arcsec pixel^{-1}. Our data were obtained from the South African Astronomical Observatory (CPT), Siding Spring Observatory (COJ), McDonald Observatory (ELP), and Cerro Tololo (LSC; Brown et al. 2013).

We obtained the images with the filters *I*-band, *R*-band, and Hα-narrow band for different purposes.

We used the *I*-band filter to obtain time-series photometry to identify variable and periodic sources. We obtained 2400 images with the *I*-band in a field centred at RA(J2000.0) = $06^{\mathrm{h}}07^{\mathrm{m}}53^{\mathrm{s}}.57$ and Dec.(J2000.0) = $-06^\circ21'59''.4$ over a period of 23 d, from 2016 December 1 to 23. Overall, we monitored a total of 6843 sources in a field, with *I*-band apparent magnitudes ranging from ∼ 14 to ∼24 mag. We took sets of 10 images with 180 s of integration per image, with an observational overhead of approximately 1.5 h. Finally, an observational cadence of 30 min between each set of 10 images was achieved.

We also obtained *R*-band and Hα narrow-band photometry of Mon R2 in order to construct colour–magnitude and colour–colour diagrams. For Hα and *R*-band data, we obtained 18 and 20 exposures, respectively, 600 and 300 s each, in the second half of December 2016. We detect 915 sources in Hα and 2355 objects in *R*-band, for a total of 844 targets with (*R* −Hα) colours. A colour image of the Mon R2 Cluster based our *I*-band, *R*-band, and Hα data taken with LCOGT is shown in Fig. 1.

2.1.2 Spectroscopy with GS

The determination of stellar mass and age in Mon R2 by photometric colour indexes is difficult due to the intrinsic differential extinction in the field. However, from the spectral types, we can obtain the effective temperature and intrinsic photospheric colours of the targets using

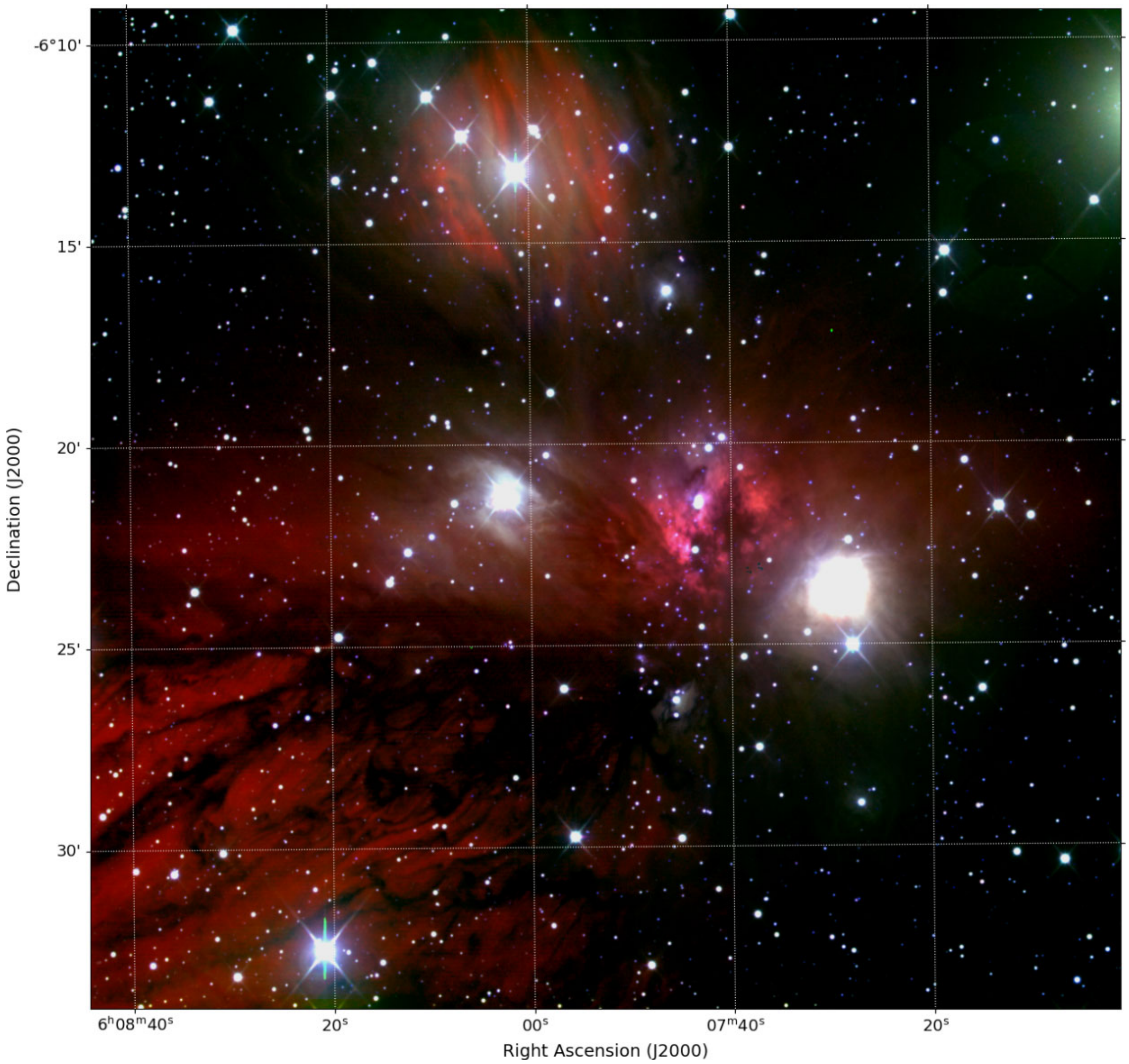

Figure 1. Image composite of the young stellar cluster Mon R2, based on *I*-band (blue), *R*-band (green), and Hα (red) data taken with LCOGT Sinistro 1-m telescopes.

calibration tables. The latter allows us to correct the photometry for extinction, enabling a more accurate determination of the mass and age of the targets. We observed Mon R2 with the Gemini Multi-Object Spectrograph (GMOS) in the multi-object mode from GS. We divided the photometry field in 16 sub-fields according the FOV of GMOS. We observed the cluster in three different programs over 3 years (programs ID GS-2017B-Q-39, GS-2018B-Q-204, and GS-2019B-Q-121) covering 12 sub-field (see Table 1 and Fig. C1). For these three programs, we used the R150 grating, which delivers optical spectra between 450 and 1100 nm with a resolving power R≈630. Our GMOS targets have *I*-band magnitudes in the 15–22 range, and were observed with integration times ranging from 5 to 11.5 min, to reach typical signal-to-noise ratios (S/N) of 50.

Data were processed in the standard way (CCD processing, aperture tracing, aperture extraction, wavelength calibration and sky subtraction), using the GMOS-Gemini package within IRAF, as in Orcajo et al. (2019). For each mask, we obtained three sets

Table 1. Details of each GMOS mask employed. In successive columns, we show the number of sub-field (according the Fig. C1), program ID, integration times (exptime), and the number of spectra obtained (n).

Sub-field	Program ID	Exptime (s)	n
01	GS-2019B-Q-121	420	20
02	GS-2019B-Q-121	420	20
03	GS-2017B-Q-39	330	19
04	GS-2018B-Q-204	435	21
05	GS-2017B-Q-39	300	26
06	GS-2018B-Q-204	435	25
07	GS-2018B-Q-204	435	31
08	GS-2018B-Q-204	690	26
09	GS-2018B-Q-204	680	25
10	GS-2018B-Q-204	435	25
11	GS-2018B-Q-204	690	24
12	GS-2017B-Q-39	330	30

of images consisting of one flat-image (called 'flat'), one CuAr lamp-image ('arc'), and one science-image ('sci'). Each set was processed individually and manually. The flats were normalized and corrected for overscan and gaps between CCD's. The slits were recognized in the flat from the gradient method and then this information was applied to the arc and sci images. Pixel-to-wavelength transformations were found using arc image calibration. Each slit was analysed individually and the results were checked until the optimal transformation was found. Sci images were corrected for overscan, flat, bad pixels, and pixel-to-wavelength transformation. Spectral extractions were interactive and spectrum was separated into a single file. The spectrum is the result of the combination of three reduced spectra, achieving an improvement of $\sim \sqrt{3}$ in the S/N. Also, we obtained telluric spectra, which were used to minimize the atmospheric contamination. We were able to obtain 297 spectra in the 12 masks employed.

2.2 Public data sets

In our study of Mon R2, in addition to our own data, we also used different public multiwavelength and multitechnique data sets, which we describe below.

2.2.1 *Pan-STARRS*

The Panoramic Survey Telescope and Rapid Response System (Pan-STARRS) is an innovative wide-field astronomical imaging and data processing facility developed at the University of Hawaii's Institute for Astronomy (Kaiser et al. 2002, 2010; Chambers & Pan-STARRS Team 2018). Chambers & Pan-STARRS Team (2018) provides an overview of the fully implemented Pan-STARRS System. The first telescope of the PanSTARRS Observatory is the Pan-STARRS Telescope #1, (Pan-STARRS1 or informally PS1). The PS1 survey used a 1.8-m telescope and a 1.4 Gigapixel camera to image the sky in five broadband filters (g, r, i, z, and y). The PS1 survey covers the entire Northern sky and extends to the South to declination -30° contains a wide range of magnitudes with millimagnitude accuracy (Tonry et al. 2012; Magnier et al. 2020). We used the data from DR2 and added a small fraction of sources with DR1 (about 15 per cent). We downloaded the data from website.[1] DR1 occurred on 2016 December 19 and DR2 on 2019 January 28. DR2 shows improvements over DR1, but both were necessary to cover all our LCOGT sources (some of these sources only had complete data, or the necessary flags, in DR1, but not in DR2; Sinha et al. 2020). We matched the PS1 sources in the g, r, i, z, and y-band filters with the sources obtained in the LCOGT field. We use the mean PSF magnitude from each filter with its associated uncertainty.[2] Sources with missing photometric errors in the catalogue were discarded. In Section 3.3.5, we explain how we select the data.

2.2.2 Gaia

The *Gaia* EDR3 represents a major and the newest release for the *Gaia* mission. The data were collected during 34 months started in 2014 and contain high-precision parallaxes and proper motions. The parallaxes and proper motions were derived from *Gaia* observations alone. These data releases cover sources brighter than $G = 21$ mag. The EDR3 presents an increment of 30 per cent in parallaxes precision and doubled the precision of proper motions respect to the previous release (GDR2; Gaia Collaboration 2018,2021; Lindegren et al. 2021; Bailer-Jones et al. 2021). First, we used the GDR2 data, then we worked with EDR3 and checked the improvements. We matched the *Gaia* sources downloaded from the EDR3 archive page[3] with sources obtained from the LCOGT field. We used the *GAIA* data to determine the proper motions and distances from Mon R2. In Section 3.3.4, we explain how the data were collected.

2.2.3 Spitzer

With the goal of studying the membership of sources to the cluster and the incidence of circumstellar material on stellar rotation, we used *Spitzer*-IRAC colours, which are particularly good disc indicators (see Section 3.3.3). To build a catalogue with the *Spitzer*-IRAC photometry data for our sample, we first obtained the data from the *Spitzer Enhanced Imaging Product*s (SEIP) Source List on a box with 1800 arcsec centred at RA=$91^{\circ}.94417$ and Dec.=$-6^{\circ}.38306$ (Equinox J2000) from the IPAC Infrared Science Archive (IRSA).[4]

We followed the recommendations of the 'Spitzer Enhanced Imaging Products Explanatory Supplement[5]' (section 1.1.2) to obtain the most reliable fluxes. However, the second recommendation, adopting FLUXFLAG $= 0$ to exclude sources that may be affected by nearby, saturated sources or nearby extended sources. This eliminated most sources located in a circular area of radius $\sim$8.5 arcmin from the cluster centre. For this reason, this recommendation was not followed. On the other hand, we chose the data with FLUXTYPE $= 1$ and used the 3.8 arcsec diameter aperture with its associated uncertainties for the IRAC channels; this makes a cut-off at SRN$\geq$3.

Furthermore, IRAC provides the photometric data in flux, which were transformed to magnitudes using the equations acquired from the same supplement in table 4.6. For these transformations, we used the zero points 280.9, 179.7, 115.0, and 64.9 Jy for fluxes $I1 = [3.6]$, $I2 = [4.5]$, $I3 = [5.8]$, and $I4 = [8.0]$, respectively.

On the other hand, we found two works with *Spitzer* data not included in the IRAC database. Gutermuth et al. (2009, hereafter G9) presented an uniform mid-IR imaging and photometric survey of 36 young, nearby, star-forming clusters and groups, including Mon R2. They used IRAC data and calibrated with *Spitzer* Science Center Standard Basic Calibrated (SSC BCD) pipeline. Kryukova et al. (2012, hereafter K12) identified protostars from nine star-forming molecular clouds within 1 kpc and Mon R2 is one of them. They extracted photometry from *Spitzer* surveys using point-spread function (PSF) fitting photometry techniques.

We cross-matched the data in the three samples mentioned above finding a good agreement among fluxes of coincident sources (within errors). Then, we constructed an unique table prioritizing data according their sources, as follows: the *Spitzer* SEIP data, G9, and K12 data. Thus, the *Spitzer* SEIP data were complemented with 48 sources from G9 and 1 from K12. The final catalogue contains 983 targets with both 3.6 and 8.0 μm data and is shown in Table F1. For completeness the 4.5 and 5.8 μm fluxes are also included, even though they are not used in the analysis. In addition, we note that

[1]https://catalogs.mast.stsci.edu/panstarrs/

[2]Some photometric values in the PS1 catalogue do not have an associated error.

[3]https://gea.esac.esa.int/archive/

[4]https://irsa.ipac.caltech.edu/Missions/spitzer.html

[5]http://irsa.ipac.caltech.edu/data/SPITZER/Enhanced/SEIP/docs/seip_explanatory_supplement_v3.pdf

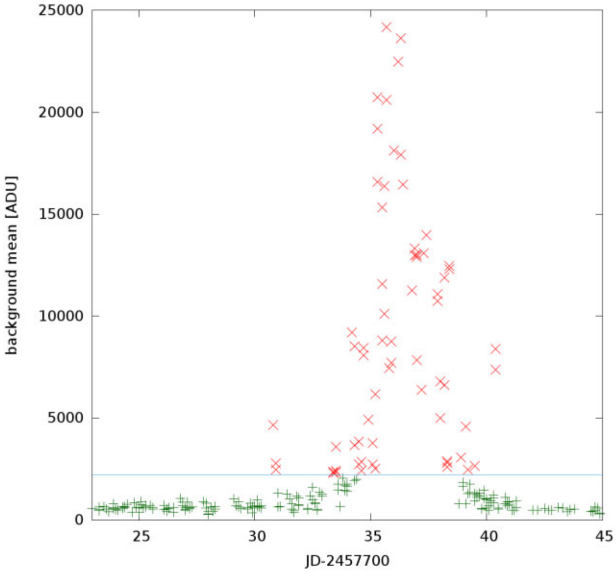

Figure 2. Mean statistic in two background sectors from each *I*-band master images. Red X symbols depict the poor-quality images (high background), while the green + signifies the good-quality images, i.e. mean <2200 ADU (see text).

the *Spitzer* SEIP, G9, and K12 data sets virtually show a 100 per cent agreement in terms of disc identification.

3 RESULTS AND ANALYSIS

3.1 LCOGT imaging data

LCOGT delivers the images processed with the BANZAI pipeline (McCully et al. 2018) as FITS multi-extension files, together with a catalogue of sources detected Source Extraction and Photometry and the bad pixel mask.[6] This photometry was not deep enough ($I_{\rm max}\sim$ 18.5 mag) to detect all objects of interest; therefore, so we decided to apply our own photometry and object search using the the tasks provided by the software IRAF, DAOFIND and APPHOT. Saturation occurred near $I\sim 12$ mag and the completeness limit was $I\sim 22.61$ mag. Where I is the I-instrumental corrected for an approximation of ZeroPoint obtained with the PS1 matched data in I-band. I is a correction for filter change, but it is not an absolute photometry

From the 2400 images obtained in *I*-band, only 1560 were useful. Some poor-quality images showed very low S/N, poor tracking or focus, etc. In order to identify poor-quality images, we studied and analysed statistically two background sectors on master images created from the median of 10 consecutive individual images with very few bright sources. We considered that if the mean of background sectors is great than 2200 ADU (3σ above the mean value of the images with the best background), the background is too bright and the S/N is too low to be useful and thus we discard all the individual images in the master image. In Fig. 2, we depict the statistic study, a gap of almost 4 d in the time-series due to bad images was unluckily obtained. To obtain a sample containing even the faintest objects, we created a super image combining all 1560 good frames in *I*-band and applied the DAOFIND package to obtain their coordinates. Finally, with the coordinates obtained, we applied aperture photometry to the 1560 individual images with the PHOT task of the APPHOT package. Finally, we cross-matched the LCOGT sources with others catalogues (*Gaia* EDR3, PS1, *Spitzer*), which drastically reduced the number of spurious sources.

[6]https://lco.global/documentation/data/BANZAIpipeline/

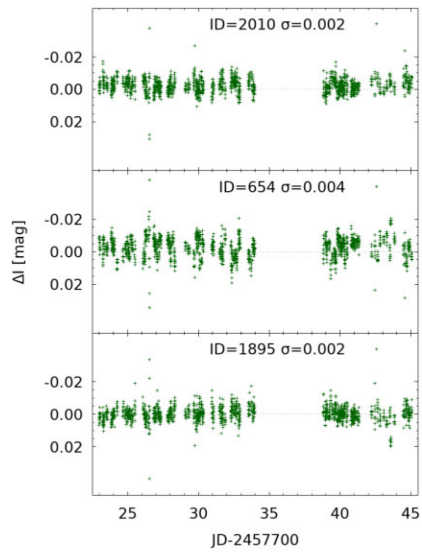

Figure 3. Differential magnitudes (Δi) versus Julian Day for three non-variable stars with the lowest photometric standard deviation. The magnitudes in i_{PS1}-band are: ID 2010 = 14.616 ± 0.004, ID 654 = 13.924 ± 0.011, and ID 1895 = 14.726 ± 0.001. Δmag is calculated between a star and the average of the three stars. The reference star has $i_{PS1}=14.442$ mag and the σ symbol is the amplitude of light curve.

3.1.1 *Differential photometry and lightcurves*

We calculated the differential photometry of the 6843 sources respect to a mean reference star, which was constructed by the averaging the fluxes of the three stars with the lowest photometric variations and resulted in 14.422 mag in the *i*-band from PS1. These reference stars were selected because they have extremely consistent differential photometry between them, indicating that they are intrinsically non-variable. Light curves of these non-variables stars are shown in Fig. 3. Each light curve was generated with the 1560 *I*-band images obtained in 23 consecutive days. The gap in the time-series is due to the discarding of bad images (see Section 3.1).

We reached $rms < 0.001$ mag, which allows us to identify variable stars with amplitudes as low as 0.01 mag. From this well-sampled and well-calibrated time-series data, we are able to find photometric periods between 0.2 and 16 d. In bottom Fig. 4, we show the mean photometric error per magnitude in the *i*-band, observing that periodic stars have errors below 20 per cent, indeed, 90 per cent remain below 5 per cent of the instrumental error.

3.1.2 *Periodograms*

We used the Lomb–Scargle (LS) algorithm, described by Scargle (1982) and Horne & Baliunas (1986) and implemented in the Interactive Data Language (IDL) software to search for periodic signals in the 6843 sources detected. The LS algorithm is a variation of the Discrete Fourier Transform, in which a time-series is decomposed into a linear combination of sinusoidal functions. The maximum power in the resulting periodogram indicates the most likely period, and the height of the maximum power is associated to a false alarm probability (FAP).

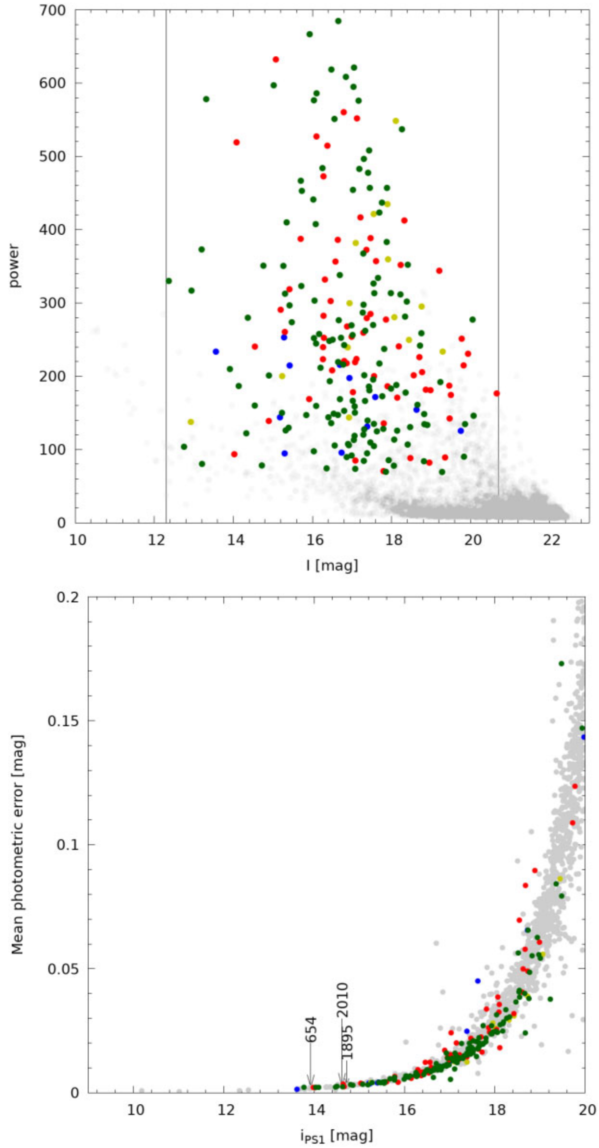

Figure 4. Top: Periodogram power versus *I*-corrected magnitudes. All sources are shown in grey; the rotation-modulated variable stars, in green; possible rotation-modulated stars, in blue; potential binary stars, in dark-yellow; and non-periodic/miscellaneous variables, in red. The black lines depict the I_c magnitude limits where we found the variables stars (outside this limits, the stars tend to be saturated or too faint to obtain accurate photometry). Bottom: Mean photometric error versus PS1 magnitude in the *i*-band with the same colours reference. Ninety per cent of the periodic stars discovered in this work have a mean photometric error of less than 5 per cent, while the remainder do not exceed 20 per cent error. In addition, we show the position of the 3 reference stars marked with an arrow indicating each ID.

For all the stars, we searched for periodic signals with periods between 0.02 and 25 d and identified the peak of the periodogram as the most likely period.

In order to identify good-quality periods in the light curves, we calculated the FAPs using the code PRACTICALLOMBSCARGLE from package ASTROPY.TIMESERIES[7] (VanderPlas 2018), which uses the default BALUEV method (similar results were obtained with the other available methods). The FAP indicates the probability of reaching a given maximum in a power spectrum due to Gaussian noise. We find that, depending on the stellar brightness, a peak power of 12–20 corresponds to a $FAP \approx 1$ per cent. However, this result is very optimistic given the assumption of purely Gaussian noise. In practice, additional sources of noise, such as those due to the changes in air-mass, produce spurious signals with peak powers up to 50 and periods close to 1 d (see top Fig. 4). Therefore, based on visual inspections and the distribution of observed peak powers seen in top Fig. 4 (top), we adopt a conservative threshold of 70 for the peak power to identify periodic stars. However, some stars with a period of about 1-d passed visual inspection, although they should be taken with caution.

We further investigated the periodicities in the light curves, with peak powers greater than 70, through the NASA Exoplanets periodogram tool[8], which also utilizes the LS algorithm but allows for an interactive inspection of multiple peaks in the periodogram of each light curve. Finally, we inspected the light curves by eye and check the spatial positions of the variables candidates. We discarded saturated stars (I_c < 12.3 mag) and stars close to diffraction spikes and the edges of the detectors. Most of these rejected stars had spurious periods of 0.5, 0.99, and 1 d.

3.1.3 Classification of variables

From the results of the periodograms and the visual inspections discussed in Section 3.1.2, we classified the variable sources with repeated photometric patterns onto the following categories:

(i) Rotation-modulated: LC with robust periodic signal, e.g. Peak Power > 70 and convincing LC from visual inspection (136 sources).
(ii) Possible: LC with marginal periodic signal, e.g. Peak Power $\sim$70 and convincing LC from visual inspection (12).
(iii) Binary: Peak Power > 70 and LC with one or more abrupt drops in magnitudes, mimicking eclipses (14).
(iv) Other: Peak Power > 70, but LC with irregular or large periodic variability but uncertain origin (64).

We are particularly interested in stars in this FOV that have a robust periodic signal because their periodicity is likely to be modulated by stellar rotation and low-mass PMS stars with photometric rotation periods have a high probability of being members of the Mon R2 cluster. We called these sources ‘rotation-modulated variables’. We separated the rotation-modulated variables in three groups according to their amplitude in greater than 0.1 mag, 0.05–0.1 mag, and lower than 0.05 mag. In Fig. 5, we show five light curves of each group per line and the rest of the rotation-modulated variables LC (grouped as above) and possible periodic in Appendix B in Figs B1–B8, respectively.

Finally, we show in appendix the binary system candidates with one abrupt drop in magnitude in Fig. B9 and more abrupt drops in magnitudes (mimicking eclipses) in Fig. B10 and the miscellaneous variables Fig. B11.

3.2 GMOS spectroscopic data

3.2.1 Spectral classification

M-type stars present molecular absorption bands mainly from titanium oxide (TiO) and vanadium oxide (VO). These bands are deeper in latter sub-spectral type. For all M-type stars the TiO band is prominent, but the VO band dominates from M5 to later types. As in

[7] http://www.astropy.org

[8] https://exoplanetarchive.ipac.caltech.edu/cgi-bin/Pgram/nph-pgram

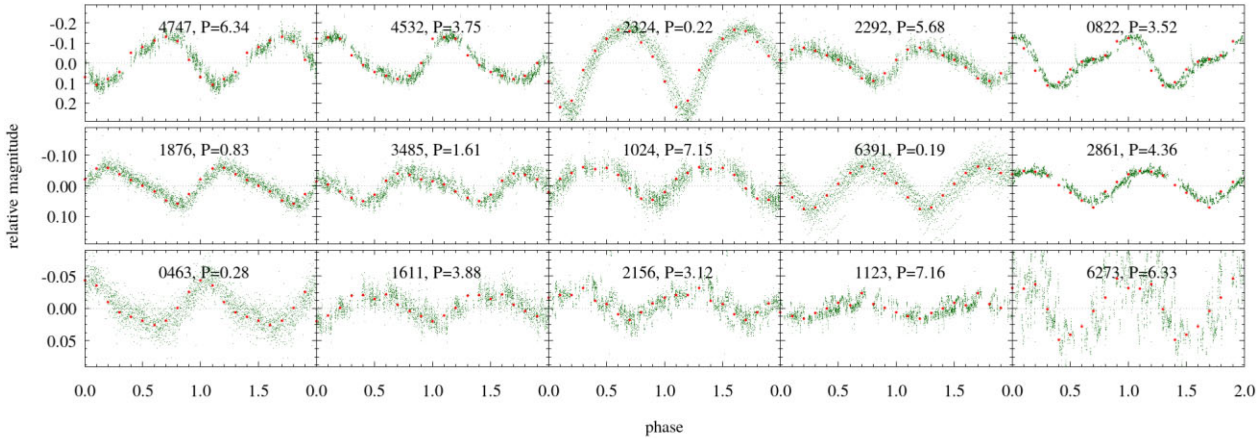

Figure 5. Phased light curves with different amplitudes. Top row: amplitude ≥ 0.1 mag. Centre row: between 0.05 and 0.1 mag. Bottom row: amplitude ≤ 0.05 mag.The light curves in each row are sorted by periodogram power. The green dots are the *I*-band data from LCOGT. The red circles are the averages of the differential magnitude every 10th of a phase. The thickness of each light curve is an approximate measure of the sample error.

Orcajo et al. (2019), we created our own internal spectral sequence of GMOS data (see Fig. 6) by comparing with published templates (Kirkpatrick, Henry & McCarthy 1991; Henry, Kirkpatrick & Simons 1994; Alonso-Floriano et al. 2015). This allows for a more direct and self-consistent comparison of all our GMOS spectra. For each of our spectra, we performed a visual comparison against the GMOS spectral sequence to determine the best match.

From the 12 GMOS fields, we obtained 297 spectra, 229 of which had enough signal to noise for spectra classification. Of these 229 objects, 140 have spectra matching M-type stars, where 58 have M2 or earlier types, and 82 have M3–M9 spectral types. The rest are likely to be K-type or earlier types, and were not classified further as the GMOS spectra lack the required resolution. For our spectral classification, we use the reference spectra obtained in the study of the cluster NGC2264 (Orcajo et al. 2019), which were taken with the same instrument. For this reason, we estimate that our spectra have an uncertainty of 1 spectral subtype based on comparisons with results from the literature.

We find that 178 of the 229 targets with useful GMOS spectra have *Spitzer* data and 86 are variables. In Table 2, we summarize the number of stars classified using our GMOS data. The sample could not be enlarged as we did not find any useful spectral classifications in the literature.

3.3 Membership

To assess whether the sources in our sample are (sub)stellar members of the Mon R2 cluster we adopted a variety of criteria based on photometric variability, disc indicators, position in H-R diagram, proper motions, and parallaxes. The different criteria are discussed below.

3.3.1 *Rotation-modulated variability*

The light curves of the variable stars classified in Section 3.1.3 as rotation-modulated variability were visually inspected, and it is notable that most of them show sinusoidal shapes. These light curves are typical of very young and active late stars (typically M-types), which present cool or hot stellar spots that cover a significant fraction of their surfaces, thus producing high-amplitude

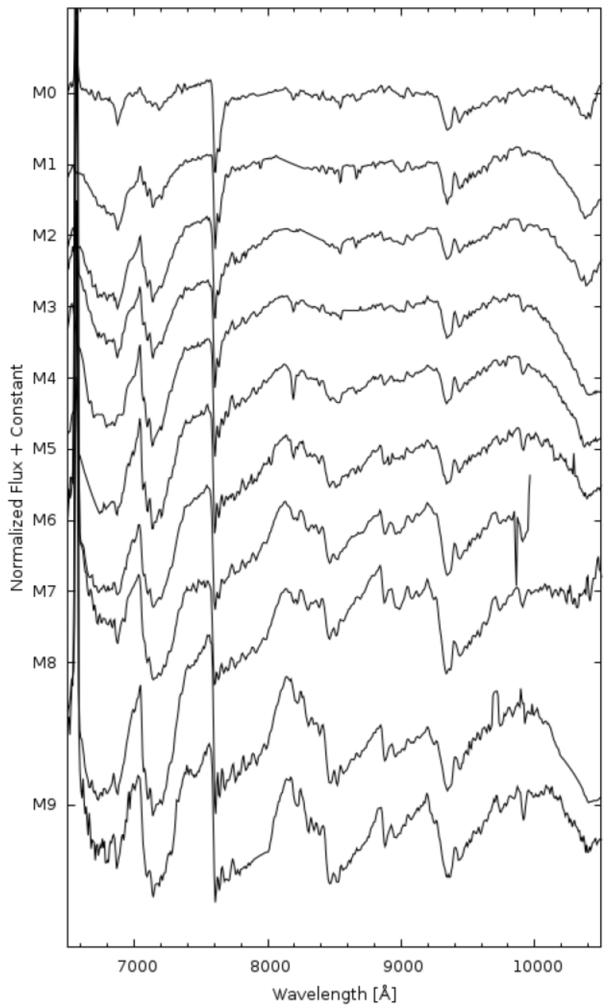

Figure 6. Spectral sequence from M0 to M9 generated with our GMOS spectra. We normalized the spectra with order 5 or 7 polynomial fits. The prominent emission line at 6560 Å is Hα. The sequence differences are most evident in the spectral range between ∼6500 and ∼8500 Å (due to TiO and VO bands).

Table 2. Number of stars according to their spectral type determined in this work. In the 'nonM' tag, we included spectral types earlier than M0, most of them are likely to be K-types.

Sub-type	Number
nonM	89
M0	28
M1	17
M2	13
M3	26
M4	15
M5	21
M6	9
M7	5
M8	3
M9	3
Total M	140

(of a few per cent or more), rotation-modulated variations. Cool spot associated with magnetic activity usually dominate the light curves of non-accreting weak-line T Tauri stars, while hot spots from magnetospheric accretion might dominate the light curves of accreting CTTSs (Herbst et al. 1994).

Field stars can also present periodic signals, but for stars in the temperature range we are working with, the amplitudes are usually less than 1 per cent of magnitude (McQuillan, Mazeh & Aigrain 2014). Considering that we can approximate the amplitude as $Amp = \sqrt{2} * rms$, the rotation-modulated stars in our sample have values above 1 per cent. Approximately 80 per cent have amplitudes between 0.01 and 0.1 magnitude, which are high for the amplitudes expected in field stars.

3.3.2 *High-scatter variables*

Using only sources with periodic variability as a membership criterion introduces a bias against accreting stars. YSOs may also have non-periodic light curves (see Appendix B), due to variable accretion. One way to find possible non-periodic variables is from the scatter of the light curve with respect to the mean magnitude value obtained. If this scatter or standard deviation is larger than the expected photometric error for a given magnitude, then the probability that a source is intrinsically variable is high. In Fig. 7, we show this standard deviation of the instrumental differential magnitude in the *I*-band versus the magnitude in the *i*-band of PS1. In Fig. 7, we also notice an overdensity of objects, mainly field stars, following a straight line. We make a linear fit to this overdensity and determine a limit above the 3σ of the fit. We note that most of the viable stars have a standard deviation of around 0.2 mag, which we interpret as the characteristic variability amplitude of the T Tauri stars in the cluster (Venuti et al. 2015). Then, we define a new membership criterion called 'high-scatter variables' ('V_hs' in Tables 3 and 4), as the sources above the 'variable limit' line in Fig. 7. Using this procedure, we identify 444 high-scatter variables. Of these 444 objects, 81 are also rotation-modulated variables based on the first criterion defined in Section 3.1.3 and 65 objects are other types of variables identified by the periodogram analysis.

3.3.3 *Disc identification*

The presence of IR excess from a protoplanetary disc can also be considered a clear indicator of young and membership to a young cluster as Mon R2 because protoplanetary discs dissipate very quickly (<1–10 Myr) and are not present in older stars in the field. The warm dust ($T \sim$ 100–300 K) in protoplanetary discs is typically optically thick and produces a characteristic mid-IR excess (Williams & Cieza 2011). Thus, the *Spitzer*-IRAC [3.6]–[8.0] colour index can be used as a robust disc indicator. These wavelengths are close to the Rayleigh–Jeans regime of the stellar photospheres and thus the photospheric colour shows little dependence on spectral types. The colour boundary between stars with and without a disc usually occur in [3.6]–[8.0] colours between 0.5 and 0.7 (Cieza & Baliber 2007; Orcajo et al. 2019). We found only 4 M-type stars with [3.6]–[8.0] colours in the 0.5–0.7 mag range and hence adopt [3.6]–[8.0] > 0.5 as disc identification criterion. We note that the disc identification criterion is only weakly affected by extinction as the median A_V of 2.09 mag determined for Mon R2 (see below in Section 3.4.2) corresponds to a reddening of just 0.07 mag in the [3.6]–[8.0] colour (Evans Neal J. et al. 2009).

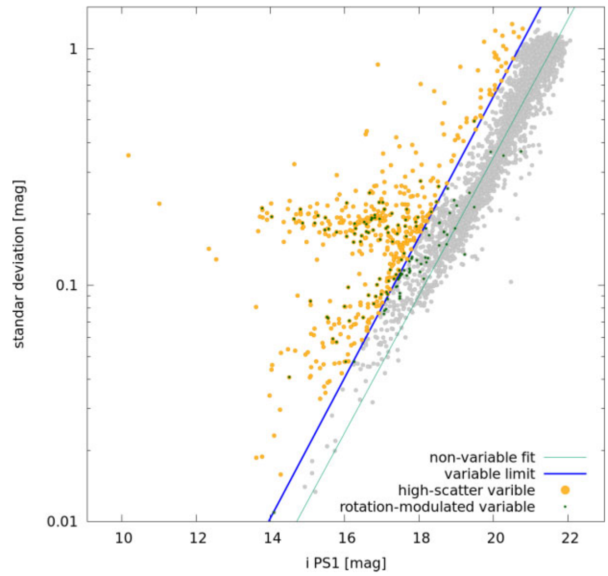

Figure 7. *i*-band (PS1) versus standard deviation in the mean differential photometry in I-band. The green line is a fit ($f(x) = 10^{(0.2912*x - 6.2837)}$) for the overdensity of objects. Above 3σ of this fit (blue line) are non-periodic variable sources, some of which are already located from the periodogram analysis. Most variable sources have a characteristic standard deviation of 0.2 mag. From this figure, we identified a total 444 high-scatter variables (yellow circles).

Table 3. Summary of membership criteria.

Flags	Description	n
ZamsFlag	Objects are located above the ZAMS isochrone.	1267
GaiaFlag	Objects with five-parameters of membership from *Gaia*: α and δ, are defined by the limits of the field obtained with LCOGT. Square 2.5 mas yr^{-1} ($\sim 2.5\sigma$) on a side around kinematic centre in $\mu_\alpha \cos(\delta) = -2.75$ mas yr^{-1} and $\mu_\delta = 1.15$ mas yr^{-1}. And ϖ between 0.888 and 1.42 mas.	206
V_type	Value 1. Objects showing periodic variability consistent with rotation modulation in this work.	136
V_hs	Objects showing high photometric scatter for given magnitude in Fig. 7.	444
Disc	Objects with IR or Hα excess consistent with disc presence	515

Table 4. Some lines of the table of candidate members. The full table is electronic. References: (1) Internal identification number. (2) RA and (3) Dec. in Equinox J2000. (4) Photometric instrumental *I*-band. (5) Instrumental rms *I*-band. (6) Differential magnitude. (7) Variability type: 1=rotation-modulated, 2=possible periodic, 3=binnary and 4=other variability. (8) Period in days. (9) Peak power of periodogram. (10) high-scatter variables (1=yes, 0=no). (11) Hα spectral line in emission (Ha), in absorption (Ha-) and 'HaCa' is Hα and CaII emission line presence. (12) Spectral Type: M1 to M9, 'nonM' for earlier spectral types and 'N' for unidentified spectra. (13) Excess in IR or Hα (1=excess, 0 = no excess). (14) Object above zams in $i - y$ colour (1=yes, 0 = no). (15) *Gaia* candidate according us parameters (1=yes, 0 = no). (16) *Gaia* source identifications. (17) *Spitzer* source identifications. (18) *Pan-STARRS* source identifications. The '-' symbol represent no sufficient data.

Id (1)	RA (2)	DEC (3)	I (4)	rms (5)	Idif (6)	V_type (7)	P(d) (8)	Power (9)	V_hs (10)	Hα (11)	SpT (12)	Disc (13)	ZamsFlag (14)	GaiaFlag (15)	Gaia_id (16)	Spz_id (17)	PS1_id (18)
6818.0	6:8:7.1856	−6:33:59.796	19.0309	0.00975613	2.02544	0	0	73	1	-	-	0	1	0	3 018 444 780 168 540 288	J060807.18-063359.3	100 120 920 299 320 610
6725.0	6:7:50.2488	−6:33:58.788	22.3372	0.162477	5.33534	0	0	10	0	-	-	-	1	0	3 018 444 569 715 178 112	J060750.25-063358.3	100 120 919 593 990 938
6781.0	6:8:18.3696	−6:33:57.06	22.5164	0.26959	5.5192	0	0	17	0	-	-	-	1	0	-	J060818.36-063356.5	100 120 920 766 011 381
6711.0	6:7:57.3912	−6:33:56.736	21.6147	0.0929442	4.61286	0	0	16	0	-	-	-	1	0	3 018 444 638 434 525 696	J060757.39-063356.4	100 120 919 890 031 543
6674.0	6:7:7.7976	−6:33:56.556	20.2315	0.0267705	3.22733	0	0	36	1	-	-	1	1	0	3 018 446 768 737 432 576	J060707.81-063355.7	100 120 917 825 831 736
6718.0	6:8:6.2544	−6:33:56.232	19.1179	0.0108045	2.11367	1	3.515	168	0	-	-	0	1	1	3 018 444 745 809 316 864	J060806.25-063355.8	100 120 920 260 641 786
6719.0	6:8:20.8008	−6:33:54.468	23.7159	0.930684	6.72568	0	0	10	0	-	-	-	1	0	-	J060820.78-063353.8	100 120 920 865 812 352
6661.0	6:7:22.6368	−6:33:52.128	19.9262	0.0223622	2.92198	0	0	54	1	-	-	1	1	0	3 018 446 940 535 925 760	J060722.64-063351.6	100 120 918 443 553 172
6683.0	6:8:2.8656	−6:33:50.256	22.8973	0.339716	5.905	0	0	12	0	-	-	-	1	0	-	J060802.86-063349.8	100 120 920 119 593 785

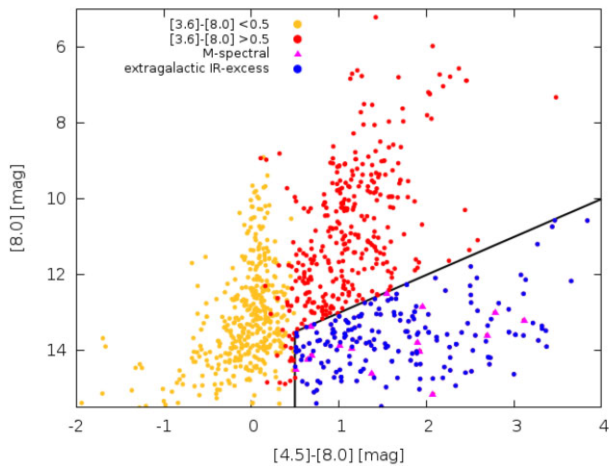

Figure 8. Diagram colour–magnitude with *Spitzer* data indicating the location of stars with and without a disc and the region occupied by extragalactic sources (Harvey et al. 2006). Note that some spectroscopically confirmed M-type stars with protoplanetary discs (red triangles) fall in the same region of the diagram as galaxies.

While the [3.6]–[8.0] colour is very useful to distinguish between stars with and without a disc, we note that extragalactic sources can have similar colours as stars with discs. In order to identify potential extragalactic objects, we adopt the criteria from Harvey et al. (2006), according to which objects with [4.5]–[8.0] >0.5 and [8.0] mag fainter than 14 – ([4.5]–[8.0]) are consider potential background galaxies (see Fig. 8). However, we find that some spectroscopically confirmed M-type stars with IR excess fall in this region of the [8.0] versus [4.5]–[8.0] diagram, implying that the *Spitzer* colours alone are not enough to distinguish between these two types of sources. On the other hand, the *Spitzer* data obtained nominally correspond to galactic objects (IRAC_OBSTYPE = 0). However, we have performed a visual inspection of the possibly extragalactic objects, discarding 10 extended sources and about 50 sources that do not appear in the *I*-band super image. The remaining sources have a high probability of being background or cluster sources.

PMS stars surrounded by protoplanetary discs can also be identified by the presence of strong Hα emission indicating accretion. Therefore, we also used our LCOGT photometry in *R*, *I* broad bands and the Hα narrow band to identified additional targets with accretion discs. We find a total of 838 sources with high quality Hα and *R* photometry (S/N > 10). From this photometry, we find that most stars have instrumental (R −Hα) colours of −3.15 (see Fig. 9 centred in 3.15). In Fig. 9, two distributions are clearly visible for objects with [3.8] − [8.0] < 0.5 (180 sources) and [3.8] − [8.0] > 0.5 (197 sources). The cut-off of the [3.8]–[8.0] < 0.5 objects around the value 0.25 is also clear. While those with [3.8]–[8.0] > 0.5 extend beyond that value. The black peaks are the objects that do not have enough *Spitzer* data (106 sources) to define the presence of a disc. In addition, the few sources with [3.8]–[8.0] < 0.5 beyond 0.25 have a high probability of having a disc due to their high emission in Hα. They could be discs with dust cavities (known as transition discs), which is why *Spitzer* does not detect it (figs 1 and 2 of Espaillat et al. 2014). Therefore, we have adopted (R −Hα) + 3.15 > 0.25 as a disc identification criterion.

Using this criterion, we added 20 sources with (R −Hα) + 3.15 > 0.25 to the list of member candidates. This criterion is very restrictive, and we seek not to contaminate our sample of stars with disc with objects without disc. Barentsen et al. (2011) shows an

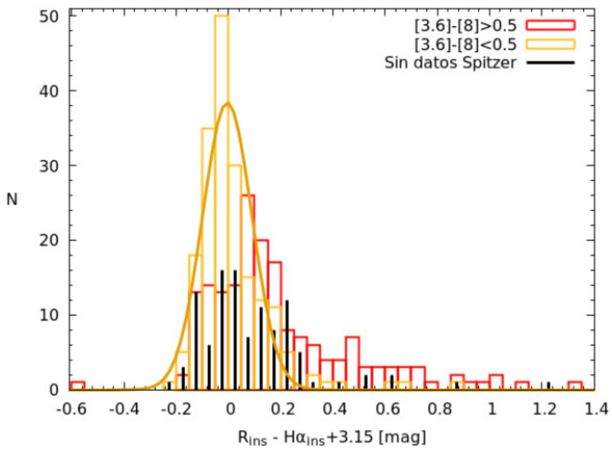

Figure 9. $(R - \mathrm{H}\alpha) + 3.15$ (instrumental magnitude) histogram with and without *Spitzer* data. Two different distributions are observed. For objects with $[3.6] - [8.0] < 0.5$, the distribution is well-defined, with a peak centred at -0.025 and to be cut off near the value 0.25, while the distribution with $[3.6] - [8.0] > 0.5$ has a peak centred at 0.05 but has a tail at values above 0.25. Objects without *Spitzer* data beyond 0.25 have a high probability of having emission in the Hα line due to the presence of a circumstellar disc.

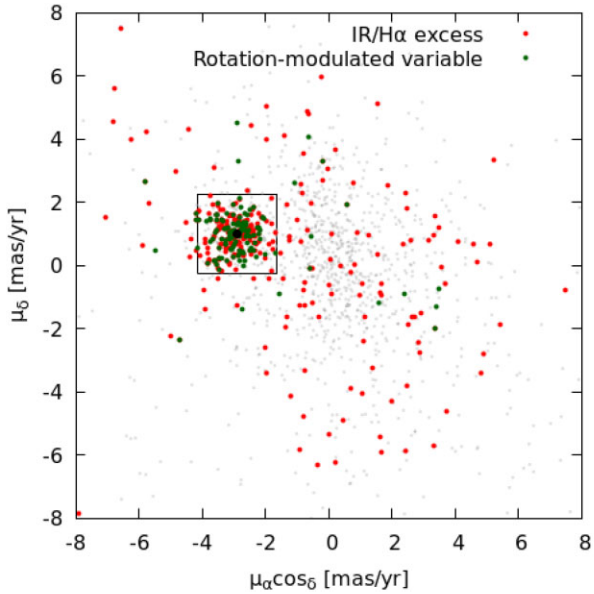

Figure 10. The proper motions from *Gaia* EDR3 data of our LCOGT sources are shown in grey (transparent) dots. The rotation-modulated variable stars are shown as green circles, while the objects with IR or Hα excess are shown as red circles. A clear conglomeration of periodic and IR or Hα excess sources is seen around $\mu_\alpha cos(\delta) = -2.75$ mas yr^{-1} and $\mu_\delta = 1.15$ mas yr^{-1}. We define a square 2.5 mas yr^{-1} ($\sim 2.5\sigma$) on a side around this kinematic centre as an additional criterion to identify member candidates.

overlap between Weak T Tauri stars and stars without Hα line. With this criterion we only detect two stars without IR-excess and with Hα emission line.

3.3.4 Gaia *distances and proper motions*

We also studied membership to Mon R2 using the five-parameter solutions (α, δ, $\mu_\alpha \cos\delta$, μ_δ, and ϖ) in the *Gaia* EDR3 database (Fabricius et al. 2021; Gaia Collaboration 2021). Based on position matches within 1 arcsec, we found $\sim$1600 coincidences with our LCOGT photometric sample with parallax and proper motions data. Regarding parallaxes, Lindegren et al. (2021) explains their limitations and the different approaches to calculate distances.

The first two parameters, α and δ, are defined by the limits of the field obtained with LCOGT. The other three parameters were constrained by statistical considerations. In Fig. 10, we plot the $\mu_\alpha cos(\delta)$ versus μ_δ plane of our LCOGT sources with EDR3 data. Clearly, a clump is appreciated around $(-2.75, 1.15)$ mas yr^{-1}. Real cluster members might have different proper motions due to dynamical interaction with other members during or after formation. Therefore, objects with proper motions outside the box can not necessarily be excluded as cluster members. Since there is no unique way to define a 'membership region' around this kinematic centre, we try to define the limits from the observed distributions. In Fig. 11, we show the distributions of proper motions. We find a well-defined bimodal distribution in $\mu_\alpha cos(\delta)$, with a peak around $\mu_\alpha cos(\delta) = -2.75$ mas yr^{-1} in addition to the peak at $\mu_\alpha cos(\delta) = 0.0$ mas yr^{-1} expected from very distant sources. We took advantage of the bimodality to set the half-width of the distributions to 1.25 mas yr^{-1} (equivalent to 2.5 σ) so that the upper limit in $\mu_\alpha cos(\delta)$ coincides the with the observed minimum between the bimodal distributions. Since the μ_δ distribution does not present this bimodality, we simply adopt the same half-width of 1.25 mas yr^{-1}. Hence, we define a square membership region with a kinematic centre at ($-$ 2.75; 1.15) mas yr^{-1} and a size of 2.5 mas yr^{-1} on each side.

To verify that the adopted ranges in proper motions are appropriate to identify new cluster member candidates, we inspect the distributions of proper motions of the rotation-modulated variable sources and/or sources with IR or Hα excess. We find that their proper motions are very consistent with the adopted ranges (see Fig. 11 bottom left and centre panel). We emphasize that excellent agreement between independent membership indicators (periodicity, IR/Hα excess, and kinematics) reinforces each one of the criteria adopted to select cluster member candidates.

In Fig. 11, we show the parallax's distribution in top right panel of the whole sample in light grey with the first selected sample in proper motion superimposed in dark grey. Even in the latter sample, there is a high dispersion that even contains negative parallaxes. Using rotation-modulated sources and/or sources with IR or Hα excess and selecting sources with errors in parallax smaller than 20 per cent, as shown in the right-bottom panel of Fig. 11, we adopt limits for the candidate member parallaxes. Thus, fitting a Gaussian to this final distribution, we adopt limits from 0.888 to 1.42 mas for the candidate member parallaxes. This values correspond to the 1.5σ limits of the distribution. We find that 206 sources fulfill the adopted five-parameter requirements from *Gaia*, 146 of them are also rotation-modulated variables and/or present IR or Hα excess.

3.3.5 *PS1 colour–magnitude diagram*

Another membership criterion is the selection of photometric sources which fall over, i.e. redder and brighter, the isochrone representing the Zero Age Main Sequence (ZAMS) of the Mon R2 cluster. To perform this task, we generated the $i - y$ versus i diagram using the PS1 data and placed the corresponding ZAMS (considering the distance modulus and mean reddening of the cluster). We selected the photometric data in both i and y bands from DR2 and DR1 (prioritizing DR2). We cross-matched 3078 LCOGT targets with i and y data from PS1 with well-defined errors in DR2 and DR1. These sources have $10.6 < i < 23.1$ mag and $10.7 < y < 20.9$ mag. We analysed different combinations of bands for the colour–magnitude

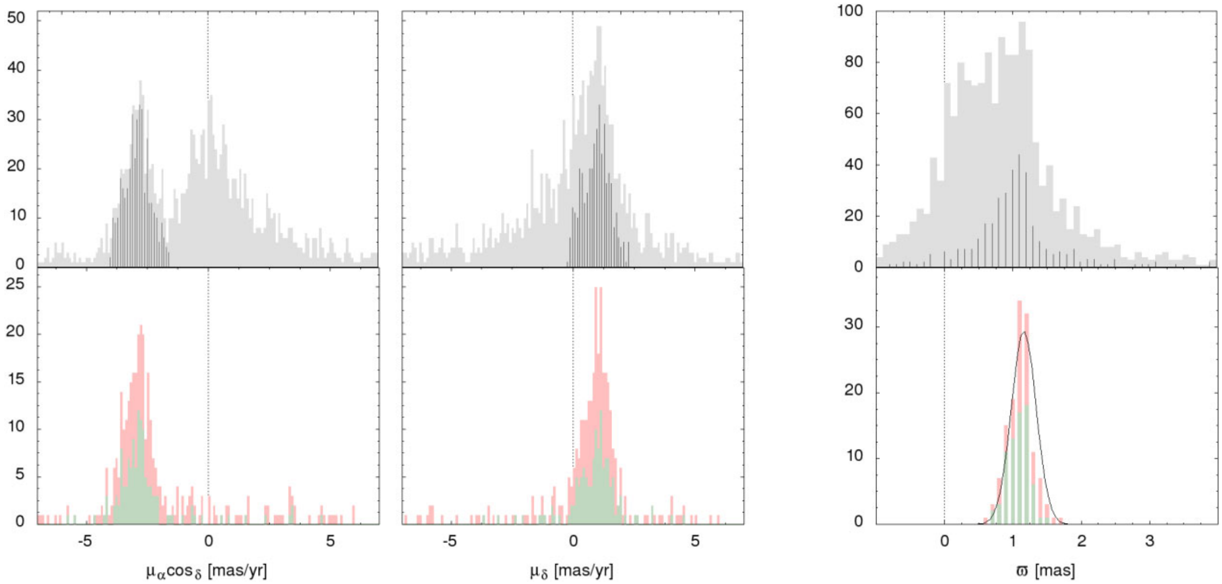

Figure 11. Member candidates from *Gaia*. **Top:** histograms of the 1600 LCOGT objects with five-parameter data from EDR3. The left-hand panel corresponds to $\mu_\alpha \cos(\delta)$, where the objects with $\mu_\alpha \cos(\delta) = -2.75 \pm 1.25$ mas yr^{-1} are shown in dark-grey. The centre panel corresponds to μ_δ, objects with $\mu_\delta = 1.15 \pm 1.25$ mas yr^{-1} shown in dark grey. The right-hand panel corresponds to the parallax data, where the dark grey fills are the ϖ of objects restricted by the proper motion limits indicated above. The dark grey objects correspond to objects inside the box in Fig. 10 and therefore cuts have been applied in both proper motion dimensions. Bottom: The same data as in the top, but limited to the rotation-modulated variables (green) and non-periodic sources with IR or Hα excess (red stacked bars). The right-hand panel shows the ϖ with the additional restriction of ϖ errors < 20 per cent.

diagram (CMD) but considered $i - y$ versus i to be the least affected by reddening (see Section 3.4.2).

We used the isochrones from the Lyon University web from Phoenix.[9] We used the 2015 BT-Settl model with $[M/H] = 0.0$ and AB photometry consistent with PS1. The BT-Settl model includes low-mass stars down to the hydrogen-burning limit and consistently couples atmosphere and interior structure. BT-Settl present $T_{\mathrm{eff}} = 15\,000$–1500 K and age of pre-sequence, starting from 1 Myr (Baraffe et al. 2015; Allard 2016). We selected four isochrones, 1, 3, and 10 Myr and the ZAMS, and we shifted them by $m - M = 9.58$ (see Section 3.4.1), $A_i = 1.315$ mag, and E($i - y$) = 0.488 mag (see Section 3.4.2). In Fig. 12, we show the $i - y$ versus i diagram with all data collected and isochrones. As all samples selected with a single membership criterion, the member candidates located above the ZAMS should be taken with caution. In particular, this sample could be contaminated by binary objects (Hurley & Tout 1998) and field stars. The uncertainty in this criterion could be as high as ≈50 per cent (see Appendix D). Therefore, we caution that this criterion should not be considered, by itself, as a reliable membership indicator and that the degree of contamination increases as the objects get closer to the ZAMS. We find that 1267 PS1 objects are located above the ZAMS isochrone. We also show the placements of *Gaia* member candidates, periodic variables, and stars with disc indicators. Their positions clearly indicate the youth of the cluster.

In Table 4, we show the Mon R2 member candidates distinguishing the different flags, i.e. rotation-modulated and high-scatter variables, star with IR or photometric Hα excess, and *Gaia* five-parameter and a summary of the membership criteria is shown in Table 3. Also, we provide the period of photometrical variations, the spectral type, and the presence of Hα in emission.

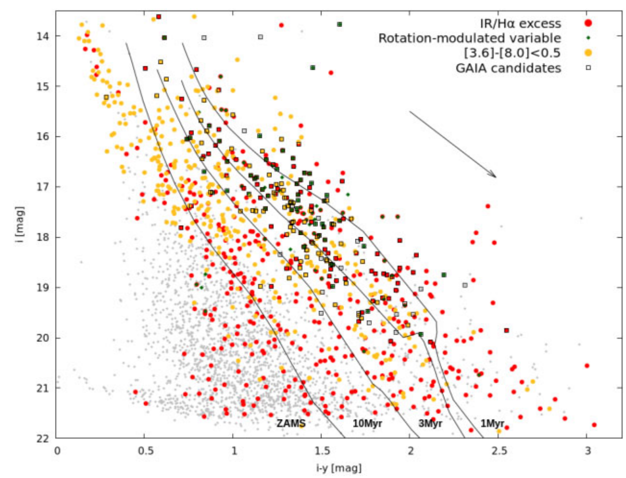

Figure 12. CMD of sources in the Mon R2 field with PS1 photometry (grey dots). We overplotted four lines depicting the 1, 3, and 10 Myr and ZAMS isochrones (see text). Note how *Gaia* candidates and periodic variables seem to concentrate around the 3 Myr line.

Finally, we obtained 1566 candidate members with at least one flags and 23 objects have five flags simultaneously (rotation-modulated, high-scatter, Disc, ZamsFlag, and GaiaFlag = 1). In addition, only one star with variability not fulfilling the membership criteria, although this may be due to insufficient information i.e. *Spitzer*, PS1 and/or *Gaia* data (source with ID = 4579).

We emphasize that all sources that meet some membership criteria are member candidates, and note that no single criterion, by itself, guarantees membership. The membership criteria should be used with caution, keeping in mind the balance between completeness and reliability. The larger the number of simultaneous membership

[9] https://phoenix.ens-lyon.fr/Grids/BT-Settl/

criteria used, the larger the reliability will be, but the lower the completeness.

There are few studies of membership in this cluster. Carpenter et al. (1997) studied Mon R2 in the near-IR (J, H, and K-band). They identified 115 member candidates with an A_V less than 11.3 mag and 309 objects brighter than 14.5 mag in K-band in a FOV of 15 × 15 arcmin^2 centred approximately at the same place as our FOV. They also estimated a total stellar population of at least 475 stars. This number is broadly consistent with our results, in which we identify 1267 objects above the ZAMS and estimate a contamination up to 50 per cent, for an estimated membership of 600 in a slightly larger FOV (26.5 × 26.5 arcmin^2). However, we note that the member candidates from Carpenter et al. (1997) might contain several deeply embedded objects that are not detected in our optical observations.

3.4 Fundamental parameters of Mon R2

After presenting the members candidates, we now discuss the fundamental parameters of the Mon R2 cluster. However, these tasks were performed somewhat iteratively. For example, the distance modulus and A_V obtained affect member candidates selected based on their position in PS1 CMD.

3.4.1 Distance

In literature, the distance to Mon R2 has been calculated mainly studying its molecular clouds and brightest stars. Racine (1968) studied the brightest stars in CMDs and obtained a distance of $d = 830 \pm 50$ pc. Herbst & Racine (1976) improved the study and found essentially the same distance. Lombardi et al. (2011) derived a distance of $d = 905 \pm 37$ pc, creating a dust column density map with 2MASS data. Schlafly et al. (2014) used the PS1 photometry data and obtained to distances, $d = 830 \pm 83$ pc for clouds near the core and $d = 1040 \pm 104$ pc for the 'Crossbones' toward the northeastern edge. Dzib et al. (2016) studied the cluster with Very Long Baseline Interferometry and derived a parallax $\varpi = 1.12 \pm 0.05$ mas that corresponds to a distance $d = 893^{+42}_{-40}$ pc. One of the most recent papers regarding the distance is Kuhn et al. (2019). They used *Gaia* DR2 to estimate the distance of 28 OCs and associations with ages from 1 to 5 Myr. For Mon R2, they found a distance of $d = 948^{+42}_{-38}$ pc.

We decided to employ the geometric and photogeometric distances calculated by Bailer-Jones et al. (2021, hereafter BJ21), for almost 1.5 billion stars. We obtained 1605 matches with distances in BJ21. We made our own distance determination using the distances calculated by BJ21 for the sources with $GaiaFlag = 1$ and $\sigma_{\varpi}/\varpi < 20$ per cent and removing a few clear outliers in distance. We obtained $d = 834 \pm 79$ pc using the mean photogeometric distance with 100 sources with a distance distribution peak at $d = 825$ pc. We adopt this latter distance, which in turn corresponds to a distance modulus of 9.58 mag.

Finally, we note that the results of GDR2 are different from those of EDR3. Also, we studied these results without taking into account variability and excess IR and the distances of EDR3 are still lower than those of GDR2 (see Appendix E).

3.4.2 A$_V$

Mon R2 is a H II region with dark nebula zones and regions of active star formation. To characterize the A$_V$ in the region, we studied the distribution of PS1 colour excesses, E($r - i$), E($r - z$), E($i - y$), E($i - z$), and E($z - y$), in stars with known spectral types. We used the extinction curves from Wang & Chen (2019, table 3; with $R_V = 3.16 \pm 0.15$ mag) and employed the intrinsic colours determined by Best et al. (2018, table 4 and 5) for M0–T9 dwarfs (also using PS1 photometry, see Appendix F2). We note that some stars resulted with (unphysical) negative E($r - i$) and E($r - z$) values. This is likely to be due to a combination of factors, including the uncertainties in the photometry and spectral types and, in some highly accreting sources, the contribution of the Hα emission to the r-band flux of late M-type stars. Also, since the A_V values obtained from colours using adjacent filters, like ($z - y$) and ($i - z$), are very sensitive to error in photometry, we decided to use E($i - y$) to estimate A_V. In Fig. 13, we show the results of A_V using the ($i - y$) PS1 colour. We find a mean A_V of 2.09 ± 1.7 mag with a few outliers outside the −1–7 mag A_V range. The distribution of extinction is the result of the differential absorption produced by the molecular cloud in which the cluster is embedded, which has significant structure.

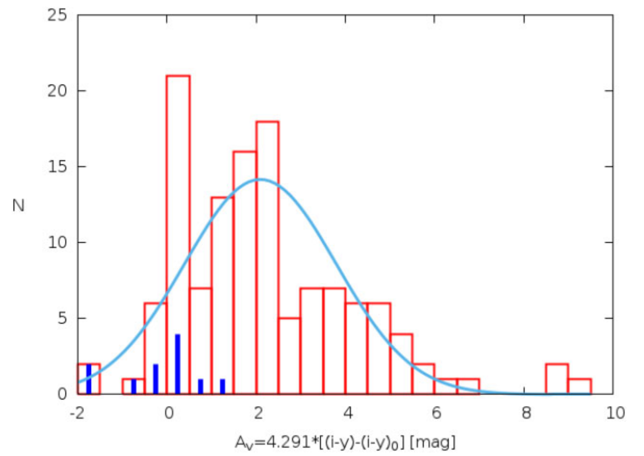

Figure 13. A_V histogram in ($i - y$) colour. In blue boxes are the spectroscopic BD with $A_V \sim 0.0$ mag. Also, we noted that three out of five objects with extreme values are variable stars. The blue spikes represent spectroscopic BD stars.

Finally, the A_V reached corresponds to a stellar extinction obtained from visible stars with spectral type found (spectral type M). Mon R2 contains areas with star-forming activity, so there are very dense clouds of up to more than 30 mag (i.e. Carpenter et al. 1997; Andersen et al. 2006; Sokol et al. 2019).

3.4.3 Age

According to the features studied in Mon R2, we observe that it is a young stellar cluster with an heterogeneous population in terms of age. Indeed, Herbst & Racine (1976) found evidence for the existence of at least two stellar groups with different ages. The first would reach an age between 6 and 10 Myrs and the second between 10^4 and 10^5 yr. The first estimate is given by the presence of B stars without emission lines, with the B1 stars located on the main sequence. The second estimate is derived from the presence of maser emission in the central region, indicating ongoing star formation. This idea is supported by Xie (1992) and Xie & Goldsmith (1994) who studied the shell structure and outflows. Carpenter et al. (1997) made an HR diagram from photometric (near-IR) and spectroscopic data and estimated a characteristic age of ≤3 Myrs.

To estimate the mean age of Mon R2, we plotted the member candidates and different isochrones on the CMD and calculate the number of members between isochrones. The age of the cluster was determined as the range with the highest density of members.

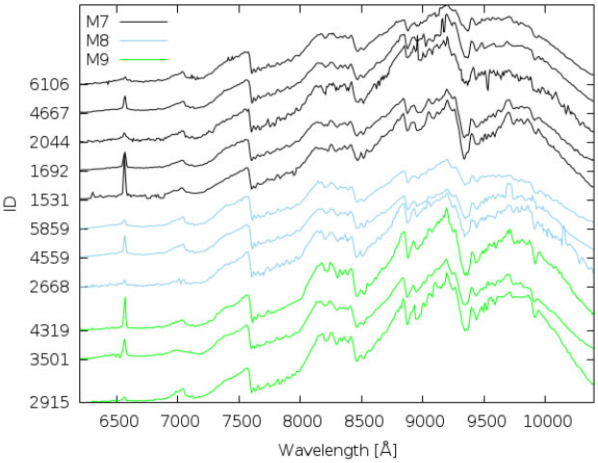

Figure 14. M7, M8, and M9 normalized spectra of BD stars. The M7 stars are in black line, M8 in light-blue line, and M9 in green line.

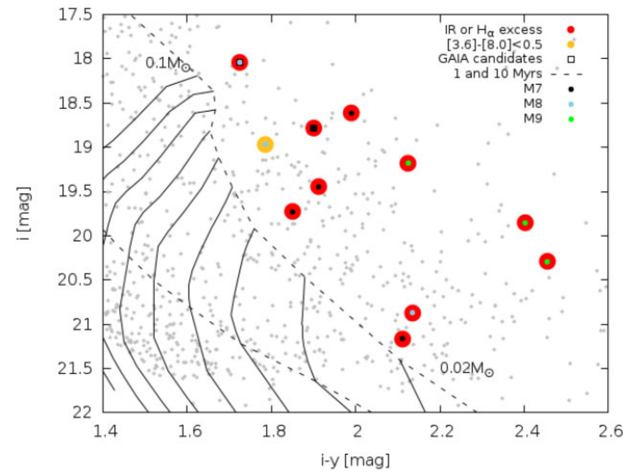

Figure 15. $(i - y)$ versus i CMD with 1 and 10 Myr isochrones and evolutionary tracks from 0.02 to 0.1 $M_{\odot}$. The position of the spectroscopically confirmed BDs are indicated by coloured circles. In this area, we find BDs candidates but we cannot confirm them as there is a contamination of low-mass stars with high reddening.

We used the isochrones described in Section 3.3.5 in i versus $i - y$ CMD, corrected by the distance and mean extinction obtained in the previous sections, in 1 Myr steps from 1 to 10 Myr. Older stars were grouped in two additional bins, 10–50 Myr and 50–100 Myr. We extracted the 248 objects that are above the ZAMS in the H-R diagram and meet at least two of the membership criteria (*Gaia* candidates, rotation-modulated variables, high-scatter variables, and stars with discs) and found that ∼50 per cent of these stars have ages < 2 Myr, and than ~ 60 per cent of the member candidates have ages between ∼1 and 3 Myr. We, therefore, adopt a mean age of 2 Myr with a characteristic dispersion of ∼1 Myr, corresponding to the size of the bins used. These results are in line with those of Carpenter et al. (1997).

3.5 Brown dwarf and brown dwarf candidates

In Section 3.2, we found 11 objects with spectral types between M7 and M9. Most of these objects clearly show Hα emission in their spectra (see Fig. 14). According to their A_V (blue spikes in Fig. 13) and position in the $i - y$ versus i CMD (Fig. 15), these M7 to M9-type objects are consistent with very young (<1 Myr) BD with little to no extinction. The youth and low extinction of these objects are likely to be selection effects because more extincted or older BD would be too faint for our GMOS observations. The eleven spectroscopically confirmed BD are listed in Table F5, while the photometric BD candidates are listed in Table F6 in Appendix F4. These photometric BD candidates are objects that occupy the same region in the $i - y$ versus i CMD (Fig. 15) as the spectroscopically confirmed BD. However, this list should be taken with a lot of caution as it is likely to be contaminated by reddened low-mass stars.

3.6 Rotation period distributions

Together with mass and metallicity, angular momentum is one of the fundamental properties determining stellar evolution. Therefore, the evolution of stellar rotation and angular momentum in young stellar clusters remains an active area of study in the field (Bouvier et al. 2014). As PMS are still contracting, they are expected to spin up as they approach the main sequence, unless they are able to efficiently drain angular momentum through star–disc interactions, a process known as disc-braking (Hartmann 2002). Indeed, previous studies have shown that PMS stars hosting protoplanetary discs tend to rotate slower than their disc-less counterparts (Herbst et al. 2002; Cieza & Baliber 2007; Orcajo et al. 2019).

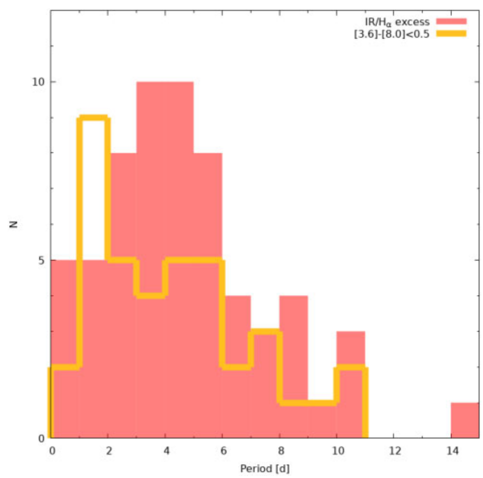

Figure 16. The period distributions of stars with (solid histogram) and without (empty histogram) a disc. K–S test p-value = 0.5946, *statistic*=0.1492, D = 0.2775, indicating that the null hypothesis cannot be discarded, but noting the trend that stars with a disc rotate more slowly than those that have lost it.

In the context of our study of the Mon R2 cluster, we investigate disc braking by selecting the rotation-modulated variable stars, for which the presence of a protoplanetary disc can be established using the IR or Hα data discussed in Section 3.3.3. Thus, we perform our analysis with 101 sources (62 of them with a disc and 39 disc-less objects). We have removed four rotation-modulated sources from this sample due to the rotation periods being even faster than the break-up speed, so these periods (p<0.35 d) would be more consistent in binary stars (Maeder 2009, chapter 2). In Fig. 16, we show the rotational period distribution for stars with and without a disc. As expected, the stars with a disc (i.e. with IR and/or Hα excess) tend to rotate slower than those without it. The two–sample K–S test (SCIPY:KS_2samp) does not reject the null hypothesis ($p-value = 0.5946$, $statistic = 0.1492$, $D = 0.2775$), probably because

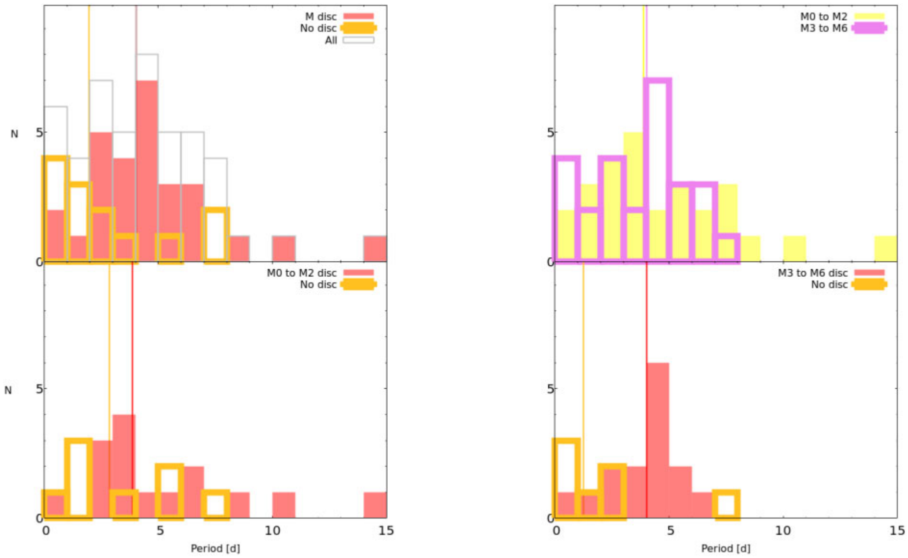

Figure 17. The period distributions for M-stars. **Top left:** period distribution for M stars with and without disc in red and goldenrod boxes, respectively, and all periodic M stars in grey line. **Top right:** period distribution for M0–M2 and M3–M6 stars in yellow and violet boxes, respectively. The distribution for M-early is flatter and spreads towards slow rotators while the distribution in M-late is more concentrated towards fast rotators with a peak between 4 and 5 d. **Bottom:** period distribution for M0–M2 (left) and M3–M6 (right) stars with and without disc in red and goldenrod boxes, respectively. In addition, in all histograms, we add the medians of each distribution respecting their colour.

the sample size is modest. Although there is a tendency in the direction predicted by disc-braking (faster rotation for discless stars), a further study is needed to increase the sample size, which could be done by spectroscopic estimations of the mass of the remaining periodic sources. Due to the differential absorption of the cluster, characterizing the mass from photometry alone can lead to large uncertainties.

In this context, the distribution shown in Fig. 16 could also be explained by a strong mass-period dependence. Work such as Rebull et al. (2020) studies the mass-period and the disc-period dependence in clusters of different ages. For clusters larger than 7 Myr, the evidence shows a strong mass-period dependence that increases with increasing age. This is expected when the circumstellar discs have dissipated and the stars increase their spin rate due to gravitational contraction until angular momentum stability is reached on the main sequence.

In our work, we only spectrally identify M-type stars, and in Fig. 17, we analysed the mass-period and disc-period dependence. In the top left panel, we separated the M-stars with and without IR/Hα-excess, and we still noticed the tendency to show the same as in Fig. 16. On the other hand, if we separated this stellar group in two between M0 and M2 and M3 to M6 (we chose this cut according to Orcajo et al. 2019), we see that there is a tendency for the M-late stars to rotate faster (as expected, e.g. Venuti et al. 2017; Orcajo et al. 2019; Rebull et al. 2020) but even so, the IR excess selection still makes a difference, i.e. stars with an excess tend to rotate slower than stars without an excess in both stellar groups. However, these results are statistically poor (47 M stars) but tend to the expected ones. To broaden the sample of periodic stars according to their mass, we perform a photometric cut according to the colour of an M1 star. We show this analysis in Appendix A. The results are inconclusive because the sample is not statistically significant. On the other hand, for the BD we have not found a convincing periodical signal.

3.6.1 Comparison to other clusters

As discs dissipate in 2–3 Myr time-scales (Williams & Cieza 2011) and stars contract towards the main sequence and spin up, the distribution of rotation periods is expected to shift toward shorter periods. In order to place Mon R2 in the context of the angular momentum evolution of young stellar clusters, we compare the rotation results obtained in Section 3.1.2 with other clusters with rotation periods in a similar mass range (of $<0.5\ M_{\odot}$ equivalent to spectral type M0 and later). To do this, we gleaned the literature and found the following four clusters: The 2 Myr NGC 6530 (Henderson & Stassun 2012; Bell et al. 2013) and Orion Nebula Clusters (Naylor et al. 2009; Davies, Gregory & Greaves 2014), the 3 Myr old NGC 2264 cluster (Makidon et al. 2004; Lamm et al. 2005; Naylor et al. 2009; Affer et al. 2013; Venuti et al. 2017; Orcajo et al. 2019), and the 5 Myr Cepheus OB3b cluster (Littlefair et al. 2010; Bell et al. 2013). For the MonR2 sample, we used the sources with spectral types from M0 and later and added the sources with colours consistent with these spectral types (111 objects with $(i - y)>0.9$ mag colour reddened).

The rotation-period distribution collected for each cluster is shown in the Fig. 18. There, it can be noted that the period distribution of Mon R2 members is intermediate between NGC 6530 the ONC cluster and is consistent with the age we calculated in Section 3.4.3. Moreover, the figure illustrates how stellar members tend to rotate faster as they age, i.e. rotation distribution tend to narrow towards shorter periods, in agreement with the predictions of the disc-braking paradigm. Such distributions can be compared to Monte Carlo models to constrains the physical parameter of disc-braking. For example, Vasconcelos & Bouvier (2015) used the Monte Carlo simulations to reproduce the period distributions in young clusters assuming the hypothesis of disc-braking. Started with a bimodal distribution of periods for disc and disc-less stars and obtained results consistent with observational data in young clusters (i.e. NGC 2264, ONC). Mon R2 has a period distribution statistically similar to that of ONC (see Table 5), so it could be represented by Monte Carlo

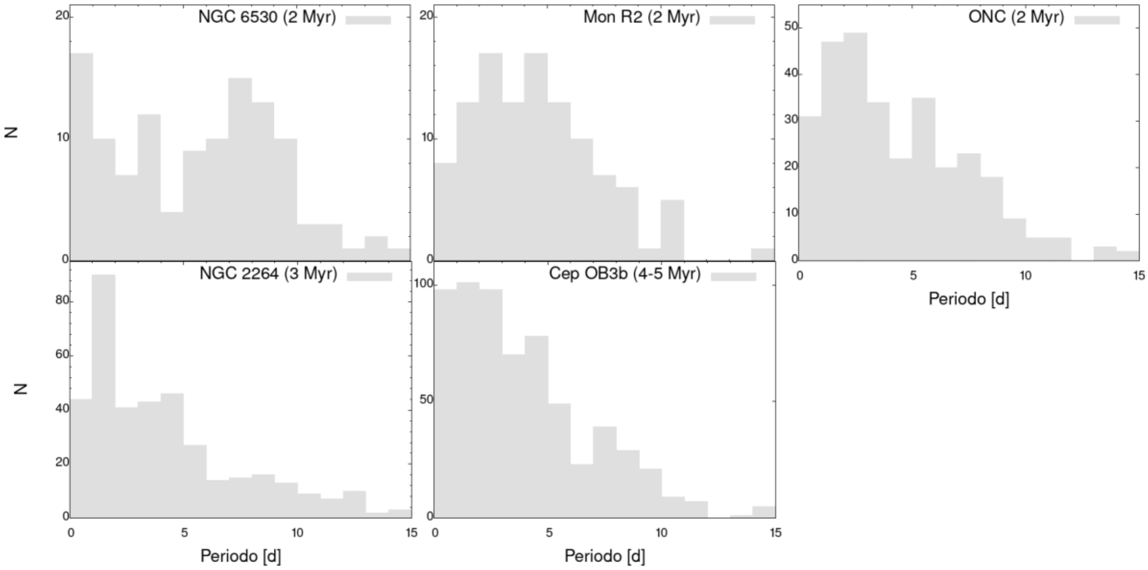

Figure 18. Period distribution of different clusters showing a progressive shift towards shortened periods with age. Samples are limited to masses less than 0.5 $M_{\odot}$, equivalent to spectral type M0.

Table 5. Statistical comparison of the cluster with the K-S test for two samples.

	NGC 6530		ONC		NGC 2264		Mon R2	
	D	$p-value$	D	$p-value$	D	$p-value$	D	$p-value$
ONC	0.14352	0.00101						
NGC 2264	0.14005	3.59388e-07	0.10231	0.01175				
Mon R2	0.17744	6.71806e-05	0.14947	0.27211	0.14613	0.01737		
Cep OB3b	0.13336	2.13161e-09	0.09295	0.00030	0.08748	0.15364	0.13974	0.01498

simulations. Therefore, the disc-braking paradigm would explain this distribution.

In Table 5, we show the values obtained with the K-S test for two samples comparing the clusters with each other. Taking as a reference a significance level of 0.05, we find that NGC 6530 is statistically different from the rest of the clusters. On the other hand, the rest of the clusters seem to follow a timeline, as ONC is statistically equal to MonR2 and NGC2264 is equal to Cep OB3b, this could also support, not only the relative age of the clusters already studied, but also the relative age of of Mon R2.

Furthermore, we observe that the younger a cluster is, the more slow rotators it contains. On the other hand, the median disc lifetimes is between 2 and 3 Myrs (Williams & Cieza 2011), this coincides with the increase of fast rotators at older ages. As the disc is lost, the star contracts and this leads to an increase in its rotation rate. If this process occurs while the star is young, then we have a fast rotator. Although we will always see a remnant of slow rotators without a disc.

4 SUMMARY AND CONCLUSIONS

In this paper, we studied and characterized the young OC Mon R2 using a multiwavelength and multitechnique approach. We used *I*-band time-series photometry to monitor the stars and to identify variability. We also used optical spectroscopy to determine the spectral types in the low-mass regime. Moreover, we identified cluster member candidates using different criteria, including variability, proper motions from *Gaia*, disc indicators (IR colours, and Hα emission) and the position in the H-R diagram. From the position of member candidates in the H-R diagram and theoretical isochrones, we also estimated the age of the cluster. Finally, we compared distribution of rotation periods of objects with and without a disc as well as the overall period distribution seen in Mon R2 to those observed in clusters of different ages. Here, we summarize our main results:

(i) We used the LCOGT Network to construct light curves for 6843 sources, each one containing 1560 differential photometry points in *I*-band. Using a periodogram analysis, we found 226 periodic stars: 136 stars consistent rotation-modulated variability and rotation periods between 0.2 and 14 d, 12 possible periodic stars, 14 eclipsing binary candidates, and 64 stars with other types of periodic variability. We also use the photometric scatter as a function of magnitude as an independent criterion to identify 444 ‘high-scatter’ variables and likely member candidates.

(ii) We spectroscopically classified 229 targets. We find that 140 objects are M-type, including 11 M7-M9 BDs, while 89 objects have K and earlier spectral types.

(iii) Of the 986 LCOGT targets with *Spitzer*-IRAC 3.6 and 8.0 μm photometry, 549 have IR colours consistent with IR-excesses above a stellar photosphere, indicating the presence of a protoplanetary disc. Using narrow-band photometry, we identified 20 additional disc candidates with Hα excess.

(iv) We matched 1591 LCOGT sources with *Gaia* EDR3 and establish the following membership criteria for Mon-R2:

(a) $\mu_{\alpha} cos(\delta) = -2.75 \pm 1.25$ mas yr^{-1}
(b) $\mu_{\delta} = 1.15 \pm 1.25$ mas yr^{-1}
(c) $0.888 \leq \varpi \leq 1.42$ mas

(v) Using sources $GaiaFlag = 1$ and have Gaia parallaxes with error smaller than 20 per cent, we have estimated a distance to the cluster of 825 ± 51 pc.

(vi) We matched 3078 LCOGT targets with the Pan-STARRS catalogue. Using the objects with known spectral types, we calculated an $A_v = 2.09 \pm 1.7$ mag for the Mon-R2 cluster using their $(i - y)$ colour excesses.

(vii) We identified a total of 1566 cluster member candidates using the following (non-exclusive) criteria:

(a) A total of 1267 PS1 member candidates above ZAMS

(b) A total of 206 *Gaia* member candidates based on proper motions and distances

(c) A total of 136 member candidates based on the rotation-modulated variability.

(d) A total of 444 member candidates based on high-scatter variability.

(e) A total of 515 member candidates based on the presence of IR and/or Hα excess.

(viii) From the position of the H-R diagram of the member candidates and the comparison to evolutionary tracks, we estimated an age of 2 ± 1 Myr for the cluster and identified 248 BD candidates.

(ix) We compared the distributions of rotation periods of stars with and without a disc signature (IR and/or Hα excess) and find tendency of stars with a disc to rotate slower, in agreement with the disc braking paradigm. We also compared the overall distribution of rotation periods in Mon R2 to that observed in clusters of different ages and find a reasonable agreement with the expectations of the angular momentum evolution in PMS stars (a progressive shift towards shorter periods with age).

ACKNOWLEDGEMENTS

We thank the anonymous referee whose comments and suggestions have helped to improve the paper significantly. We thank Tim Naylor for his recommendations on the use of his tau^2 code https://www.astro.ex.ac.uk/people/timn/tau-squared/. Santiago Orcajo and Roberto Gamen acknowledge support from grant Proyectos de Investigación Científica y Tecnológica (PICT) 2019–0344. Lucas A. Cieza acknowledges support from Agencia Nacional de Investigacio\'on y Desarrollo, Fondo Nacional de Desarrollo Científico y Tecnológico (ANID FONDECYT) grant 1211656. This work makes use of observations from the Las Cumbres Observatory global telescope network. This work is based [in part] on observations made with the Spitzer Space Telescope, which was operated by the Jet Propulsion Laboratory, California Institute of Technology, under a contract with NASA. Based on observations obtained at the international Gemini Observatory, which is operated by the Association of Universities for Research in Astronomy, Inc., under a cooperative agreement with the NSF on behalf of the Gemini partnership: the National Science Foundation (United States), National Research Council (Canada), Agencia Nacional de Investigación y Desarrollo (Chile), Ministerio de Ciencia, Tecnología e Innovación (Argentina), Ministério da Ciência, Tecnologia, Inovações e Comunicações (Brazil), and Korea Astronomy and Space Science Institute (Republic of Korea). This work has made use of data from the European Space Agency (ESA) mission *Gaia* (https://www.cosmos.esa.int/gaia), processed by the *Gaia* Data Processing and Analysis Consortium (DPAC, https://www.cosmos.esa.int/web/gaia/dpac/consortium). Funding for the DPAC has been provided by national institutions, in particular the institutions participating in the *Gaia* Multilateral Agreement. The Pan-STARRS1 Surveys and the PS1 public science archive have been made possible through contributions by the Institute for Astronomy, the University of Hawaii, the Pan-STARRS Project Office, the Max-Planck Society and its participating institutes, the Max Planck Institute for Astronomy, Heidelberg, and the Max Planck Institute for Extraterrestrial Physics, Garching, The Johns Hopkins University, Durham University, the University of Edinburgh, the Queen's University Belfast, the Harvard-Smithsonian Center for Astrophysics, the Las Cumbres Observatory Global Telescope Network Incorporated, the National Central University of Taiwan, the Space Telescope Science Institute, the National Aeronautics and Space Administration under Grant No. NNX08AR22G issued through the Planetary Science Division of the NASA Science Mission Directorate, the National Science Foundation Grant No. AST-1238877, the University of Maryland, Eotvos Lorand University (ELTE), the Los Alamos National Laboratory, and the Gordon and Betty Moore Foundation. This research has made use of the NASA Exoplanet Archive, which is operated by the California Institute of Technology, under contract with the National Aeronautics and Space Administration under the Exoplanet Exploration Program. This research made use of ASTROPY,[10] a community-developed core Python package for Astronomy (Astropy Collaboration 2013, 2018).

DATA AVAILABILITY

The IR data are available through https://irsa.ipac.caltech.edu/cgi-bin/Gator/nph-dd and https://vizier.u-strasbg.fr/viz-bin/VizieR (Gutermuth et al. (2009) and Kryukova et al. (2012). The PS1 DR1 and DR2 data are available from https://catalogs.mast.stsci.edu/panstarrs/. The Gaia EDR3 data are available from https://gea.esac.esa.int/archive/. The distance data are available from VIZIER Bailer-Jones et al. (2021). All the above-mentioned data are available through the ALADIN software (https://aladin.u-strasbg.fr/). The isochrones tables are available through https://phoenix.ens-lyon.fr/Grids/BT-Settl/. Gemini spectra will be available at the Argentinian Virtual Observatory, NOVA, at https://nova.conicet.gov.ar/. The light curves obtained with LCOGT on which this article is based will be available as online material.

REFERENCES

Affer L., Micela G., Favata F., Flaccomio E., 2012, MNRAS, 424, 11
Allard F., 2016, Reylé C., Richard J., Cambrésy L., Deleuil M., Pécontal E., Tresse L., Vauglin I.eds, SF2A-2016: Proc. Annual meeting of the French Society of Astronomy and Astrophysics. Société astronomique de France, Paris, p. 223
Alonso-Floriano F. J. et al., 2015, in Cenarro A. J., Figueras F., Hernández-Monteagudo C., Trujillo Bueno J., Valdivielso L., eds, Highlights of Spanish Astrophysics VIII. p. 441
Andersen M., Meyer M., Oppenheimer B., Dougados C., Carpenter J., 2006, AJ, 132, 2296
Astropy Collaboration, 2013, A&A, 558, A33
Astropy Collaboration, 2018, AJ, 156, 123
Bailer-Jones C. A. L., Rybizki J., Fouesneau M., Mantelet G., Andrae R., 2018, AJ, 156, 58
Bailer-Jones C. A. L., Rybizki J., Fouesneau M., Demleitner M., Andrae R., 2021, AJ, 161, 147
Baraffe I., Homeier D., Allard F., Chabrier G., 2015, A&A, 577, A42
Barentsen G. et al., 2011, MNRAS, 415, 103
Bell C. P. M., Naylor T., Mayne N. J., Jeffries R. D., Littlefair S. P., 2013, MNRAS, 434, 806
Best W. M. J. et al., 2018, ApJS, 234, 1

[10] http://www.astropy.org

Bouvier J., Matt S. P., Mohanty S., Scholz A., Stassun K. G., Zanni C., 2014, in Beuther H., Klessen R. S., Dullemond C. P., Henning T., eds, Protostars and Planets VI. Univ. Arizona Press, Tucson, p. 433
Brown T. M. et al., 2013, PASP, 125, 1031
Carpenter J. M., Hodapp K. W., 2008, in Reipurth B., ed., Vol. 4, Handbook of Star Forming Regions, Vol. I. p. 899
Carpenter J. M., Meyer M. R., Dougados C., Strom S. E., Hillenbrand L. A., 1997, AJ, 114, 198
Castro-Ginard A. et al., 2020, A&A, 635, A45
Chambers K. et al., 2016, preprint (arXiv:1612.05560)
Choi M., Evans Neal J. I., Tafalla M., Bachiller R., 2000, ApJ, 538, 738
Cieza L., Baliber N., 2007, ApJ, 671, 605
Cody A. M. et al., 2014, AJ, 147, 82
Cody A. M., Hillenbrand L. A., 2018, AJ, 156, 71
Davies C. L., Gregory S. G., Greaves J. S., 2014, MNRAS, 444, 1157
Dzib S. A., Ortiz-León G. N., Loinard L., Mioduszewski A. J., Rodríguez L. F., Torres R. M., Deller A., 2016, ApJ, 826, 201
Espaillat C. et al., 2014, in Beuther H., Klessen R. S., Dullemond C. P., Henning T.eds, Protostars and Planets VI. Univ. Arizona Press, Tucson, p. 497
Evans Neal J. I. et al., 2009, ApJS, 181, 321
Fabricius C. et al., 2021, A&A, 649, A5
Fedele D., van den Ancker M. E., Henning T., Jayawardhana R., Oliveira J. M., 2010, A&A, 510, A72
Gaia Collaboration, 2018, A&A, 616, A1
Gaia Collaboration, 2021, A&A, 649, A1
Gutermuth R. A., Megeath S. T., Myers P. C., Allen L. E., Pipher J. L., Fazio G. G., 2009, ApJS, 184, 18
Hartmann L., 2002, ApJ, 566, L29
Harvey P. M. et al., 2006, ApJ, 644, 307
Henderson C. B., Stassun K. G., 2012, ApJ, 747, 51
Henry T. J., Kirkpatrick J. D., Simons D. A., 1994, AJ, 108, 1437
Herbst W., Bailer-Jones C. A. L., Mundt R., Meisenheimer K., Wackermann R., 2002, A&A, 396, 513
Herbst W., Herbst D. K., Grossman E. J., Weinstein D., 1994, AJ, 108, 1906
Herbst W., Racine R., 1976, AJ, 81, 840
Hillenbrand L. A., Kiker T. J., Gee M., Lester O., Braunfeld N. L., Rebull L. M., Kuhn M. A., 2022, AJ, 163, 263
Horne J. H., Baliunas S. L., 1986, ApJ, 302, 757
Hurley J., Tout C. A., 1998, MNRAS, 300, 977
Irwin J., Hodgkin S., Aigrain S., Bouvier J., Hebb L., Irwin M., Moraux E., 2008, MNRAS, 384, 675
Janes K., Adler D., 1982, ApJS, 49, 425
Kaiser N. et al., 2002, in Tyson J. A., Wolff S., eds, Proc. SPIE Conf. Ser Vol. 4836, Survey and Other Telescope Technologies and Discoveries. SPIE, Bellingham, p. 154
Kaiser N. et al., 2010, in Stepp L. M., Gilmozzi R., Hall H. J., eds, Proc. SPIE Conf. Ser Vol. 7733, Ground-based and Airborne Telescopes III. SPIE, Bellingham, p. 77330E
Kirkpatrick J. D., Henry T. J., McCarthy D. W., Jr, 1991, ApJS, 77, 417
Kohno M., Koyama K., Hamaguchi K., 2002, ApJ, 567, 423
Kryukova E., Megeath S. T., Gutermuth R. A., Pipher J., Allen T. S., Allen L. E., Myers P. C., Muzerolle J., 2012, AJ, 144, 31
Kuhn M. A., Hillenbrand L. A., Sills A., Feigelson E. D., Getman K. V., 2019, ApJ, 870, 32
Lada C. J., Lada E. A., 2003, ARA&A, 41, 57
Lamm M. H., Bailer-Jones C. A. L., Mundt R., Herbst W., Scholz A., 2004, A&A, 417, 557
Lamm M. H., Mundt R., Bailer-Jones C. A. L., Herbst W., 2005, A&A, 430, 1005
Lindegren L. et al., 2021, A&A, 649, A4
Littlefair S. P., Naylor T., Mayne N. J., Saunders E. S., Jeffries R. D., 2010, MNRAS, 403, 545
Lombardi M., Alves J., Lada C. J., 2011, A&A, 535, A16
Maeder A., 2009, Astronomy and Astrophysics Library, Physics, Formation and Evolution of Rotating Stars. Springer, Berlin, Heidelberg
Magnier E. A. et al., 2020, ApJS, 251, 6
Makidon R. B., Rebull L. M., Strom S. E., Adams M. T., Patten B. M., 2004, AJ, 127, 2228
McCully C., Volgenau N. H., Harbeck D.-R., Lister T. A., Saunders E. S., Turner M. L., Siiverd R. J., Bowman M., 2018, in Guzman J. C., Ibsen J.eds, Proc. SPIE Conf. Ser. Vol. 10707, Software and Cyberinfrastructure for Astronomy V. SPIE, Bellingham, p. 107070K
McQuillan A., Mazeh T., Aigrain S., 2014, ApJS, 211, 24
Molina Lera J. A., Baume G., Gamen R., 2019, MNRAS, 488, 2158
Naylor T., Mayne N. J., Jeffries R. D., Littlefair S. P., Saunders E. S., 2009, in Mamajek E. E., Soderblom D. R., Wyse R. F. G.eds, Proc. IAU Sump. 258, The Ages of Stars. p. 103
Orcajo S., Cieza L. A., Gamen R., Peterson D., 2019, MNRAS, 487, 2937
Racine R., 1968, AJ, 73, 233
Rayner T. S. M. et al., 2017, A&A, 607, A22
Rebull L. M., 2001, AJ, 121, 1676
Rebull L. M., Stauffer J. R., Cody A. M., Hillenbrand L. A., Bouvier J., Roggero N., David T. J., 2020, AJ, 159, 273
Rebull L. M., Wolff S. C., Strom S. E., 2004, AJ, 127, 1029
Rigliaco E., Natta A., Testi L., Randich S., Alcalà J. M., Covino E., Stelzer B., 2012, A&A, 548, A56
Scargle J. D., 1982, ApJ, 263, 835
Schlafly E. F. et al., 2014, ApJ, 786, 29
Shu F. H., Adams F. C., Lizano S., 1987, ARA&A, 25, 23
Sim G., Lee S. H., Ann H. B., Kim S., 2019, J. Kor. Astron. Soc., 52, 145
Sinha T. et al., 2020, MNRAS, 493, 267
Sokol A. D. et al., 2019, MNRAS, 483, 407
Tonry J. L. et al., 2012, ApJ, 750, 99
VanderPlas J. T., 2018, ApJS, 236, 16
Vasconcelos M. J., Bouvier J., 2015, A&A, 578, A89
Venuti L. et al., 2015, A&A, 581, A66
Venuti L. et al., 2017, A&A, 599, A23
Wang S., Chen X., 2019, ApJ, 877, 116
Williams J. P., Cieza L. A., 2011, ARA&A, 49, 67
Xie T., 1992, PhD thesis, UMass Boston
Xie T., Goldsmith P. F., 1994, ApJ, 430, 252
Zhong J., Chen L., Wu D., Li L., Bai L., Hou J., 2020, A&A, 640, A127

SUPPORTING INFORMATION

Supplementary data are available at *MNRAS* online.

suppl_data

Please note: Oxford University Press is not responsible for the content or functionality of any supporting materials supplied by the authors. Any queries (other than missing material) should be directed to the corresponding author for the article.

APPENDIX A: PERIOD DEPENDENCE

For the disc braking study, as our sample of spectral types is small, we decided to analyse our periodic sources by separating them on the basis of mass determination by photometry. For this, we use PS1 photometry and make the $(i - y)$ versus $(z - y)$ colour–colour diagram shown in Fig. A1. At $(i - y) = 1.077$, we have placed the boundary between M1 and earlier and M2 and later stars. This colour limit is calculated from the values obtained by Best et al. (2018, tables 4 & 5) and corrected by the mean A_V obtained in this work. We have superimposed the spectroscopic sources of M2 and later to contrast this limit. Note that, as the reddening is unidirectional, the sample of M2 sample and the later stars can be contaminated by the reddened earlier stars. In contrast, the sample of M1 and earlier stars will be much less contaminated. Finally, we obtained 36 early and 97 late stars.

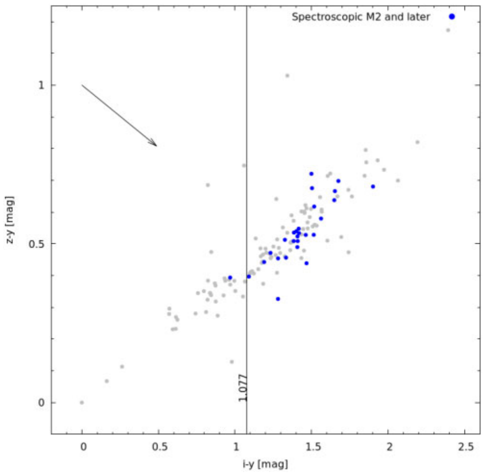

Figure A1. Colour–colour diagram for rotation-modulated variable sources with PS1 photometry (133 stars) in grey circles. In blue circles are the spectroscopic M2 and later stars. At $(i - y) = 1.077$ mag is the photometric limit between M1 and earlier and M2 and later stars. The arrow at the top left is the extinction vector, corresponding to mean $A_V = 2.09$ mag.

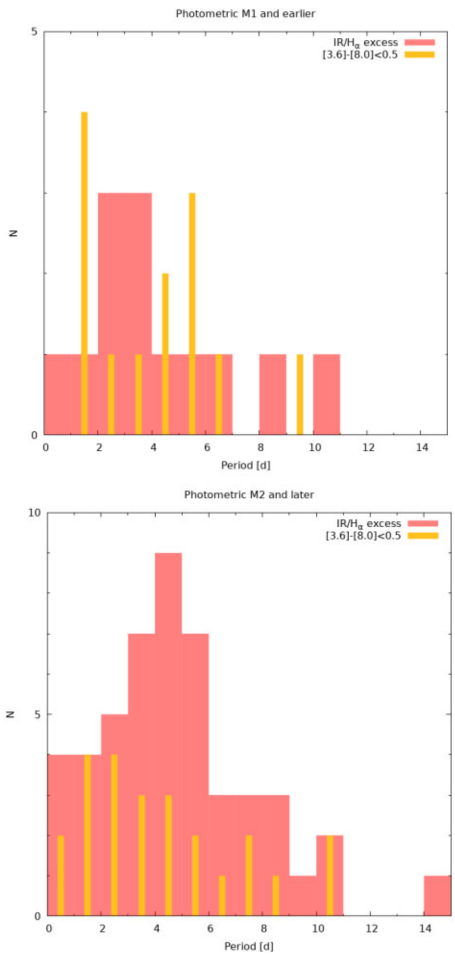

Figure A2. The period distributions of stars with (solid histogram) and without (spikes histogram) a disc. **Top:** M1 and earlier stars according to the cut shown in Fig. A1. **Bottom:** M2 and later stars according to the same cut.

Table A1. KS-test for photometric samples.

Sample	Disc	No disc	No disc data	$p-value$	D	*statistic*
M1 & earlier	13	13	6	0.999	0.533	0.154
M2 & later	49	24	24	0.629	0.411	0.175

Once both samples were selected, we split them between with and non-disc sources to make the histograms of the period distribution shown in Fig. A2 (we removed sources with periods shorter than 0.35 d). We apply the KS statistic for two samples to obtain the results shown in Table A1. The statistical results are inconclusive due to the small sample size. However, in the case of M2 and later stars, there is a tendency for those with a disc to rotate more slowly.

APPENDIX B: ROTATION-MODULATED STARS AND OTHER VARIABLES

In this section, we show the rest of the rotation-modulated variables of the Mon R2, from Figs B1 to B8.

Moreover, in our sample, we found LC with abrupt drops in magnitude that we interpret as eclipsing or occultation (by circumstellar material) events. Ten of them show multiple events during the observation time, and four stars show just a unique dimming (see Figs B10 and B9, respectively). Other targets in our sample show irregular photometric variations (see Fig. B11) that might be due to variable accretion and/or stellar activity. However, the aim of this work is to characterize the Mon R2 cluster, so the objects presented in this section have not been studied in depth but might be interesting for follow-up studies. Nevertheless, the morphologies found in our sample are varied and similar to those described by other authors, such as Cody et al. (2014), Venuti et al. (2017), Cody & Hillenbrand (2018), and Hillenbrand et al. (2022). They classified their variable stars according to two parameters: the stochasticity (or alternatively, periodicity) that they called Quasi-periodicity (Q), and the degree of flux asymmetry named Flux asymmetry (M). This statistical study yielded different types of variability. Certainly this classification starts with purely periodic stars due to the presence of star spots. But there are multiperiodic objects possibly due to the combination of star spots in binary pairs. In addition, there are long time-scale objects that present a variability on time-scales longer than 25 d. Other types of variability that exhibit asymmetry could be due to a combination of periodicity of spots with non-periodic changes of longer duration or due to unstable cycle-to-cycle variability, are the quasi-periodic symmetric. The quasi-periodic dipper variable exhibits variability due to stellar occultation by circumstellar material. There are also aperiodic dipper variables. On the other hand, burster (B) variables correspond to objects with erratic but discrete accretion bursts. Finally, the stochastic (S) variables present non-repetitive variability patterns with relatively symmetric excursions around a mean brightness. We recommend reading the work of Hillenbrand et al. (2022) for more details. Finally, in Fig. B12, we compared non-variables stars with periodic stars with similar magnitude for three different magnitudes bright, medium and faint magnitude. This study presents a high sensitivity that allows us to find variability in faint sources.

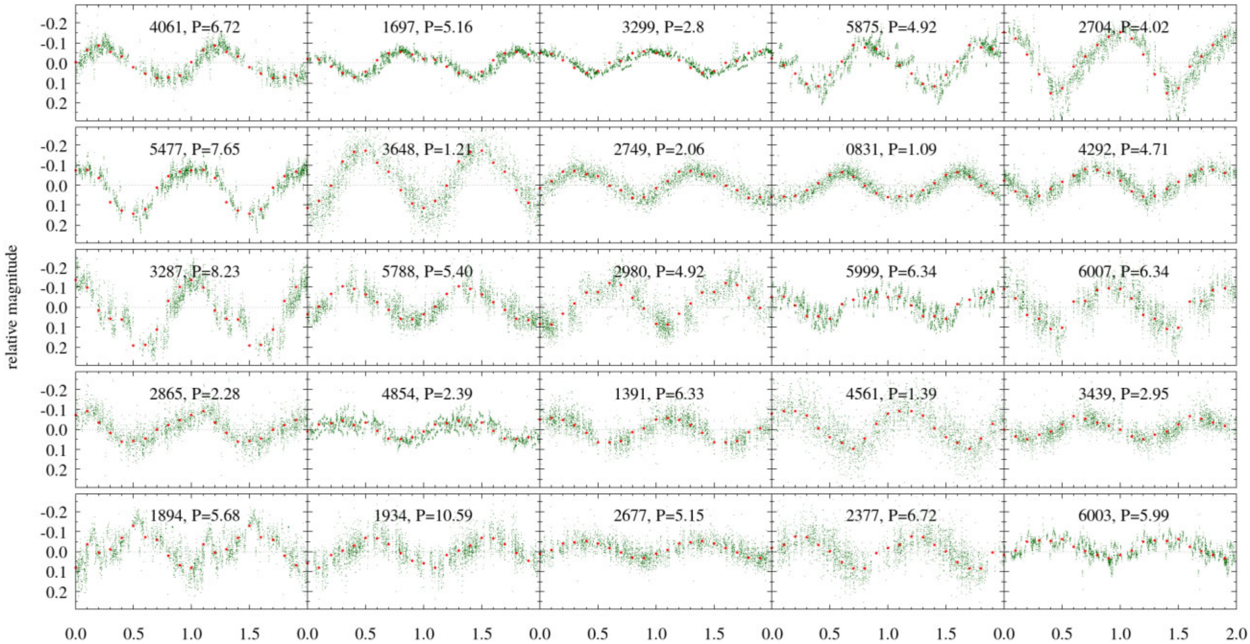

Figure B1. Phased light curves with amplitude ≥0.1 mag, ordered by periodogram power. The green dots are the *I*-band data from LCOGT. The red circles are the averages of the differential magnitude every 10th of a phase.

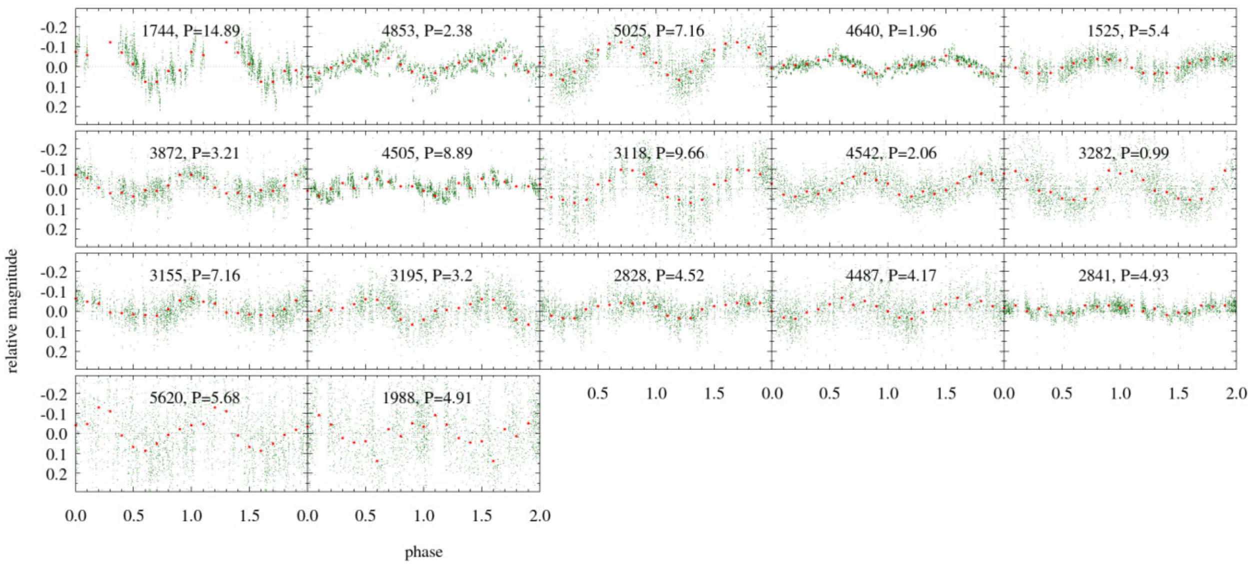

Figure B2. Continued Fig. B1.

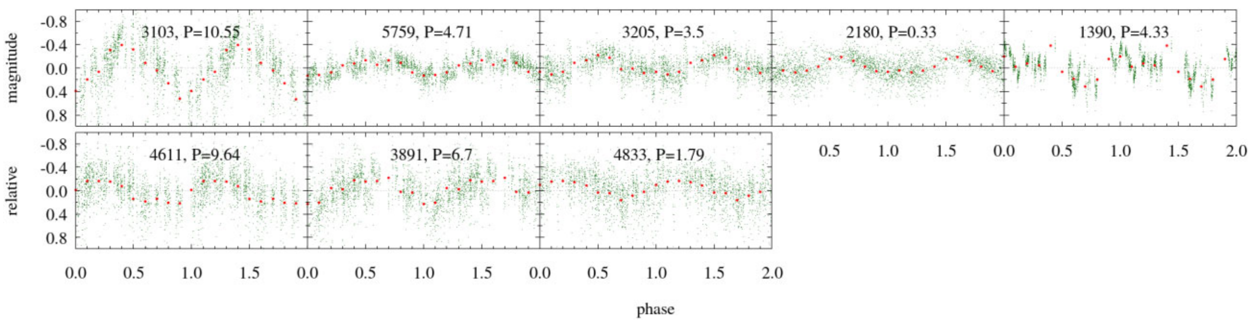

Figure B3. Continued Fig. B1.

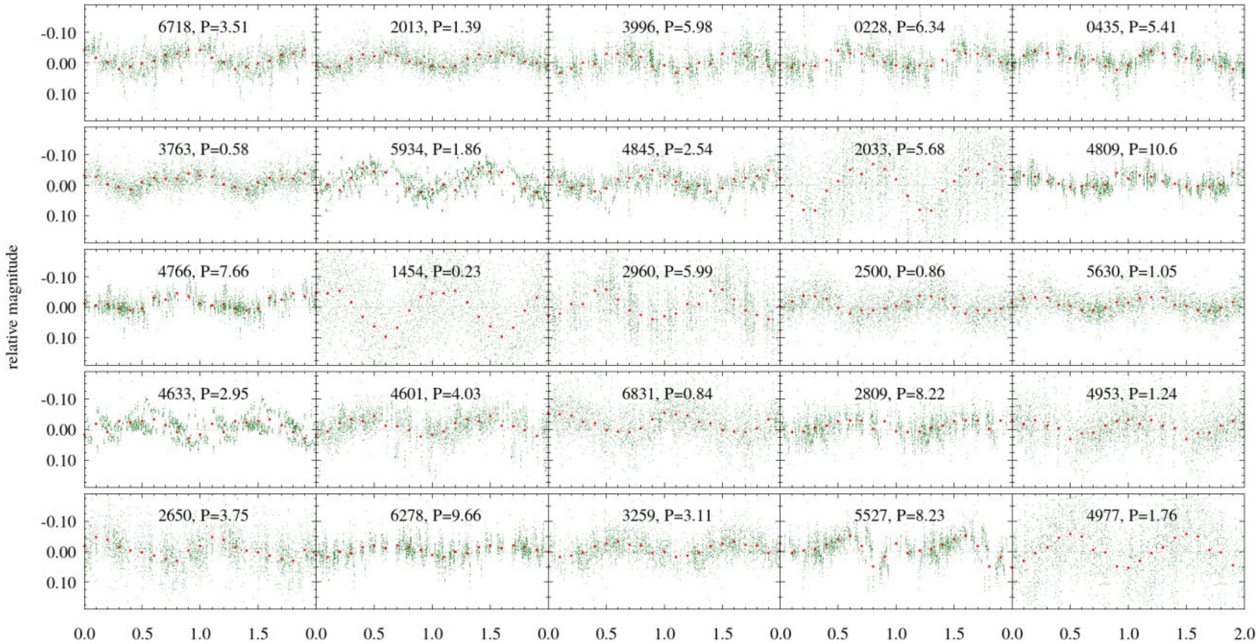

Figure B4. Phased light curves with amplitude between 0.05 and 0.1 mag, ordered for periodogram power. The green dots are the *I*-band data from LCOGT. The red circles are the averages of the differential magnitude every 10th of a phase.

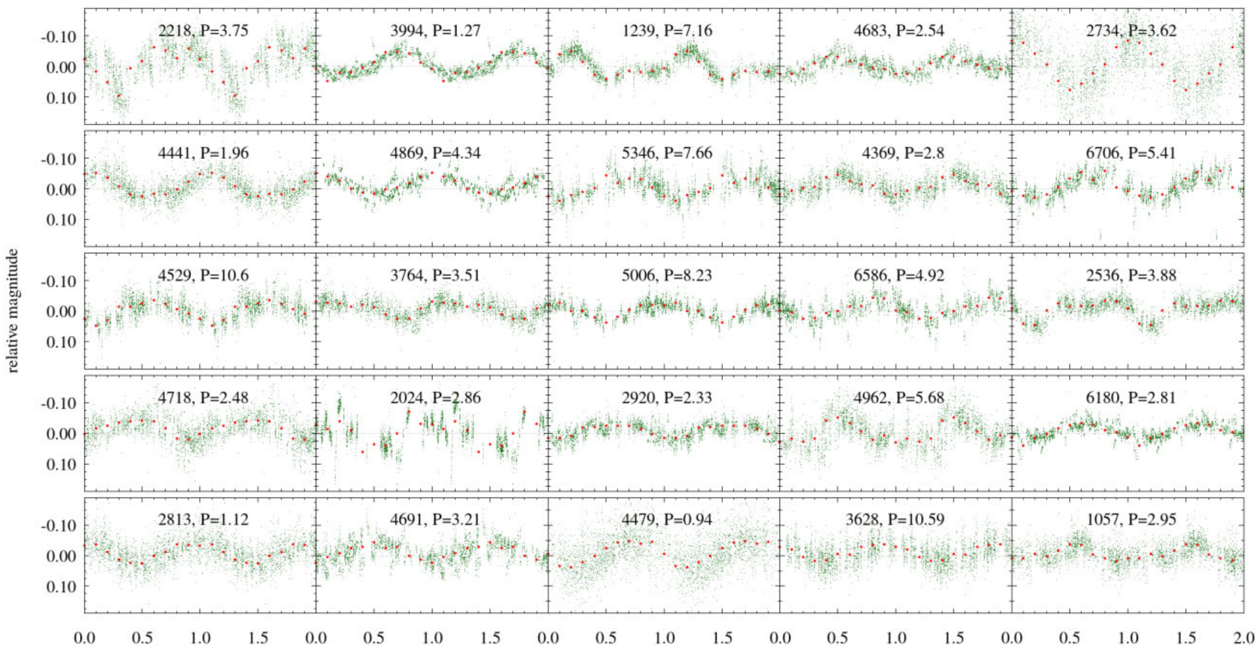

Figure B5. Continued Fig. B4.

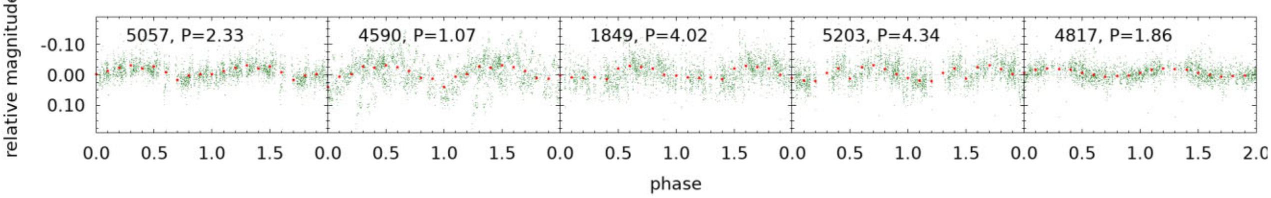

Figure B6. Continued Fig. B4.

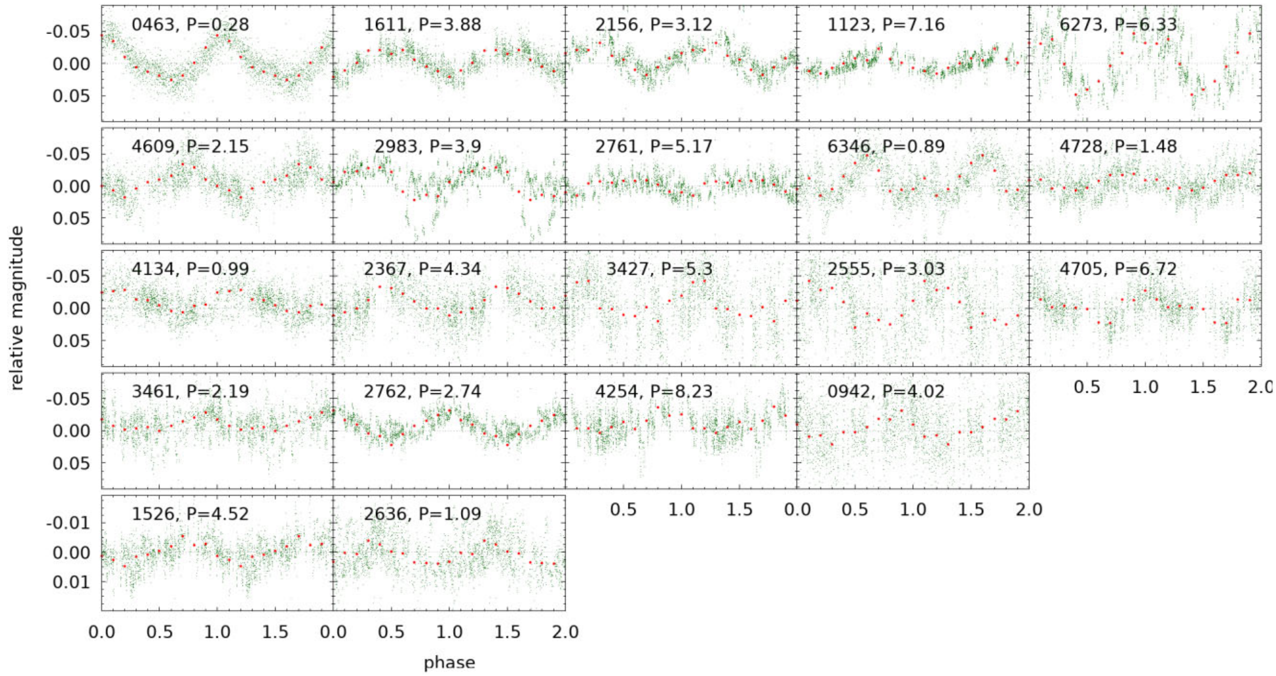

Figure B7. Phased light curves with amplitude ≤ 0.05 mag, ordered for periodogram power. The green dots are the *I*-band data from LCOGT. The red circles are the averages of the differential magnitude every 10th of a phase.

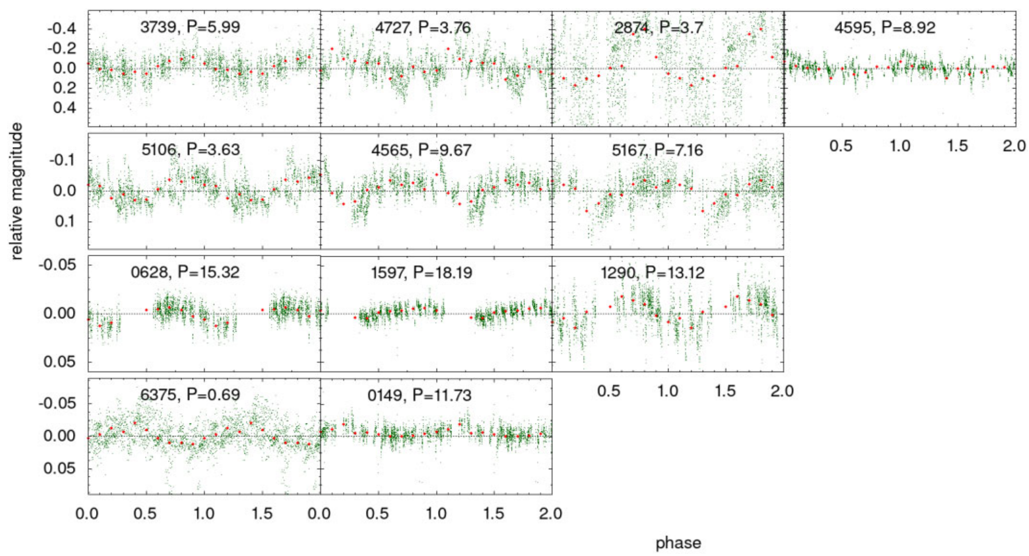

Figure B8. Phased light curves of'possible' periodic stars, ordered for periodogram power and amplitude. The green dots are the *I*-band data from LCOGT. The red circles are the averages of the differential magnitude every 10th of a phase.

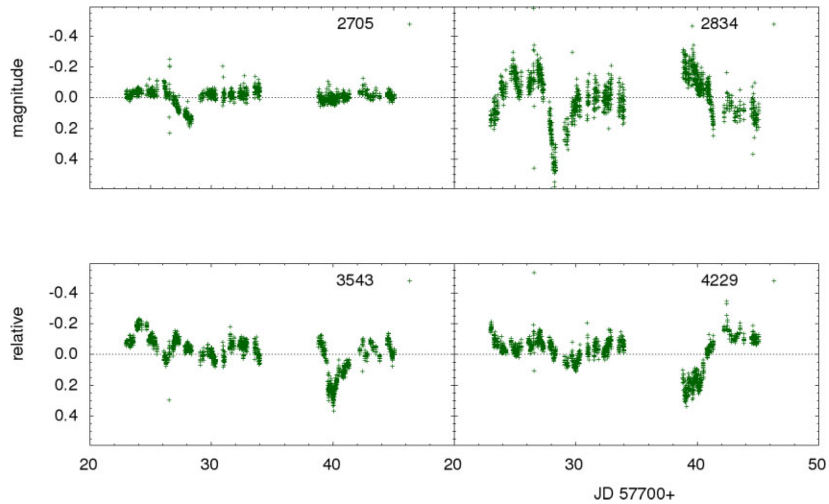

Figure B9. Light curves of stars with one eclipse during our observation time.

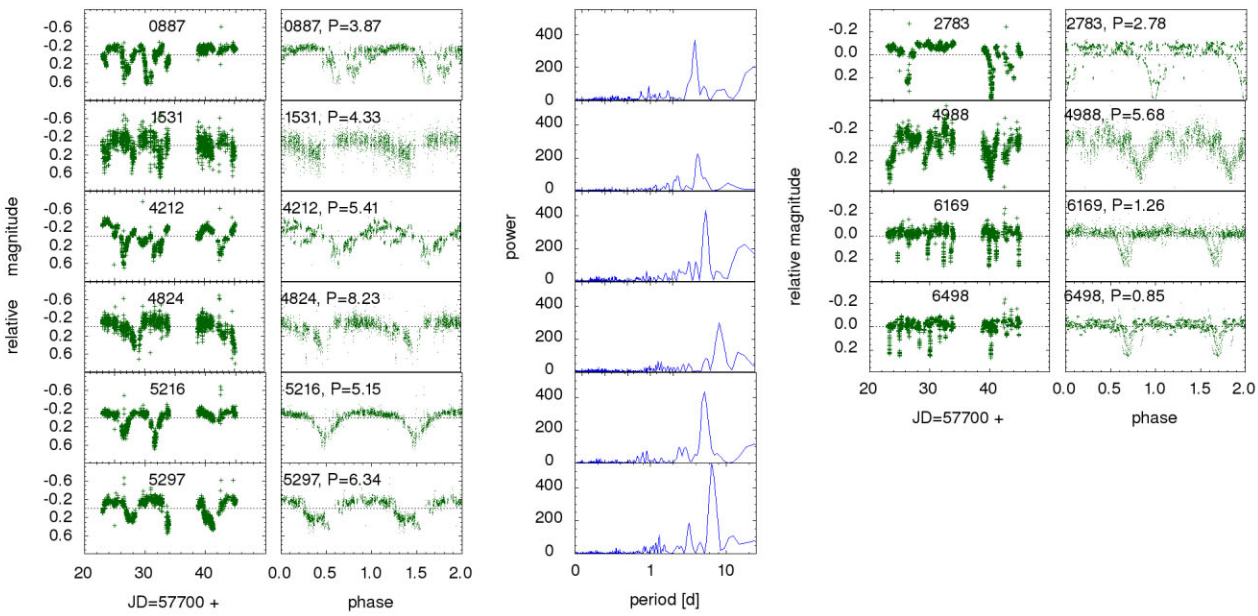

Figure B10. Light curves of stars with multi-eclipses during our observation time. We presented the periodogram of best power peak, the other stars not have a clear visual power peak in periodogram.

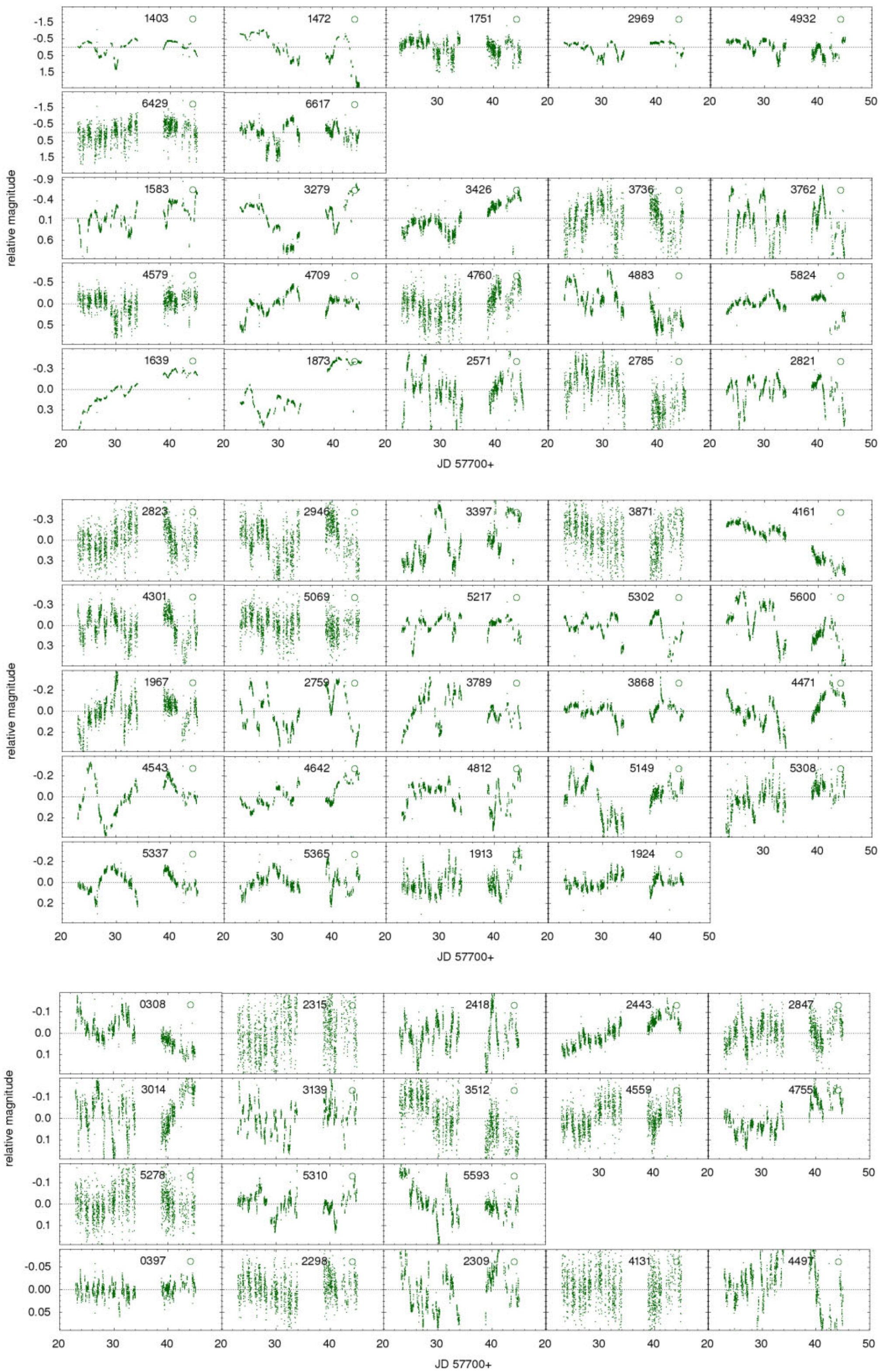

Figure B11. Light curves of no periodic variability.

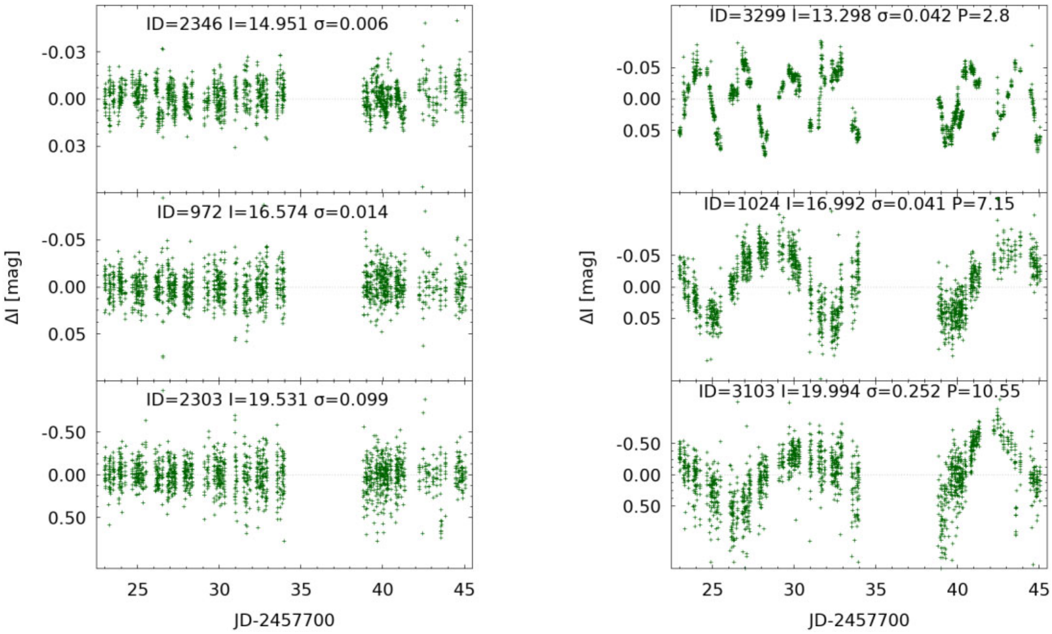

Figure B12. Non-variables versus periodic stars with similar magnitude for three different magnitudes bright, medium, and faint magnitude. The LC of 3299, 1024, and 3103 are in Figs B1, 5, and B3, respectively.

APPENDIX C: GEMINI'S FIELDS

In Fig. C1, we show the fields of each mask used with Gemini, and the objects studied in each of them.

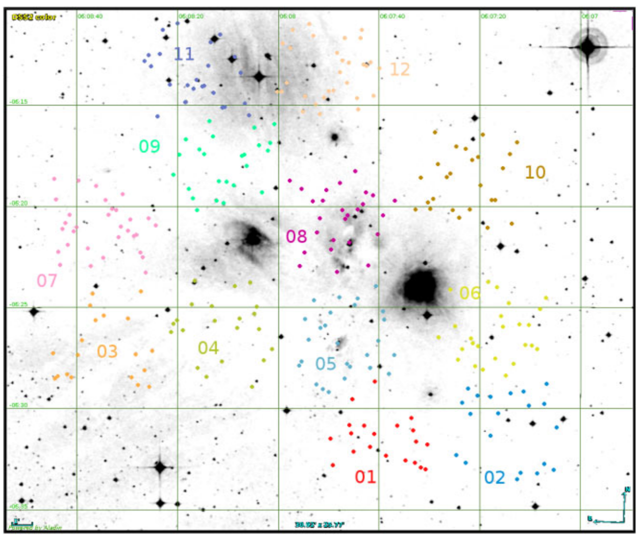

Figure C1. Sub-fields of Mon R2 where GMOS masks were placed. Spectral targets are represented with coloured circles according to their sub-field. The background images correspond on the Digitalized Sky Survey 2 from Aladin sky atlas.

APPENDIX D: ZAMS CRITERION

Sources above the ZAMS may be contaminated by field stars, so establishing this feature as a membership criterion leads to the largest uncertainties among the criteria. Then, to estimate this uncertainty, we performed the same procedure detailed in Section 3.3.5 using the same LCOGT FOV at the same galactic latitude but shifted in longitude (coordinates in ICRS: RA = $06^{h}09^{m}40^{s}.08$ DEC = $-05°57'17''.5$). We obtained 641 objects from PS1 photometry (in the *i* and *y*-bands) above ZAMS, compared to the 1267 objects in the Mon R2 field. Thus, assuming that this sample contains no Mon R2 members and that they are only field stars, we estimate the uncertainty for this criterion could be as high as ≈50 per cent (due to contamination). In Fig. D1, we show the HR diagram with the sources of this new field that we called 'Adjacent FOV' and the members of Mon R2. A also performed a similar analysis by taking another field at the same galactic latitude and obtained a very consistent result.

However, while the comparison between the number of stars above the ZAMS in both fields (control field and Mon R2 field) is based on the assumption that the stellar density of both fields is the same, this is not necessarily true since the Mon R2 field contains the young cluster. An alternative way to obtain the contaminant rate is to calculate the ratio of stars above the ZAMS to those below it in the control field. Then, to obtain the expected number of contaminants in the Mon R2 field, we multiply this ratio by the number of sources below the ZAMS in this field. This method also suffers from some complications because of the differential extinction, which is not present in the control field. To alleviate this effect, we restrict the comparison to objects brighter than 21 mag in the PS1 magnitude to reach a reasonable completeness level in Mon R2. Using this cut, we find 558 and 2690 sources above and below the ZAMS in the control field and 1345 objects below the ZAMS in Mon R2. This give

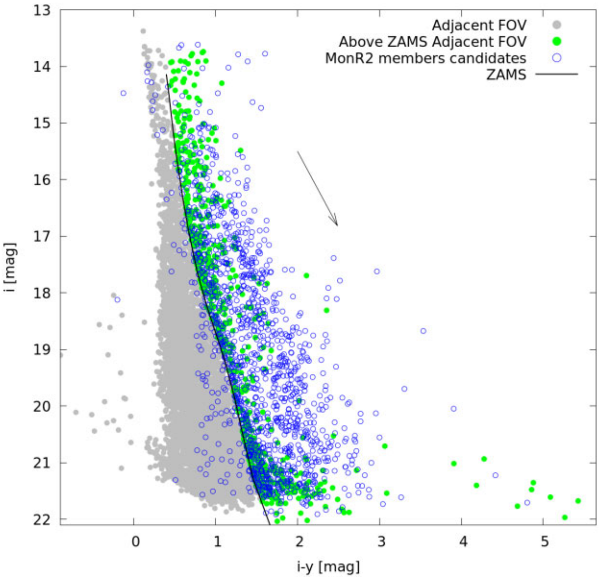

Figure D1. CMD in *i-y* versus *i* (PS1 DR2 photometry) of sources outside the studied Mon R2 field (grey and green), overlapped with the candidate members (blue). In addition, we mark the ZAMS with a black line. The contamination is clearly concentrated over the ZAMS.

an estimate contamination of (558/2690)∗1345 = 279 stars. These 279 stars correspond to 26 per cent of the 1074 member candidates observed above the ZAMS in Mon R2 (including the *i*-mag restriction mentioned above). We therefore estimate that the contamination of Mon R2 members selected from their position in the H-R diagram to be between 1/4 and 1/2.

APPENDIX E: OBTAINING THE DISTANCE WITH DR2 AND EDR3

For the study of the mean distance to the cluster, we have used the *Gaia* DR2 and EDR3 data. Some sources have negative parallax values, so we have also performed this study with the Bailer-Jones et al. (2018, BJ18) catalogue, associated to DR2 data and BJ21 associated to EDR3 data. For the parallax study, we have taken the sources that fulfilled at least two membership criteria and that have a parallax error of less than 20 per cent, avoiding negative parallaxes. In addition, we have analysed the distributions of rotation-modulated variables and/or IR/Hα-excess members. The histograms in Fig. E1 show that the distribution for the DR2 data has an closer peak than the distribution for the EDR3 data, 1.05 and 1.15 mas, respectively, so DR2 locates the cluster at a greater distance.

For the distance (in pc) study, we have taken the sources with *GaiaFlag* = 1 (see Table 3) that have a parallax error of less than 20 per cent. Also, we analyse these values but taking rotation-modulated variables, IR/Hα-excess or non-variable sources, these histograms are in Fig. E2. Again, we find that the BJ18 data show larger distances than the BJ21 data. In addition, in the first column of these two panels, we overlay the sources that meet four membership flags (*ZamsFlag* = 1, *GaiaFlag* = 1, *V_type* = 1 and *Disc* = 1, Table 3). The black vertical line in each distribution indicates the peak of the distributions associated with EDR3 ($\varpi = 1.15$ mas and $d = 825$ pc).

On the other hand, the two most recent catalogues (EDR3 and BJ21) show higher precision in the data because, with the parallax constraint, more sources are obtained than in the previous ones (DR2 and BJ18). Finally, for the BJ21 photogeometric data, we observe that the peak of the non-variable star distribution coincides with the peaks of the rest of the distributions. For the geometrical data, the

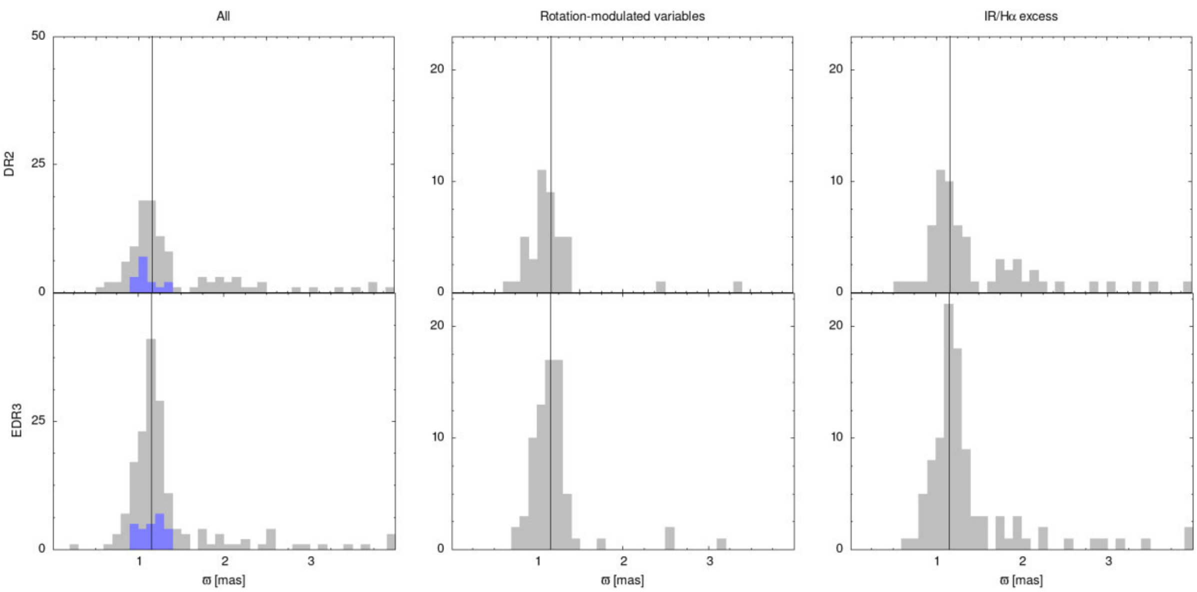

Figure E1. Parallax histograms with *Gaia* DR2 and EDR3 data for sources that fulfill at least two membership criteria and that have a parallax error of less than 20 per cent, avoiding negative parallaxes. The vertical line is located at the $\varpi = 1.15$ mas. The blue boxes are the sources with four membership flags simultaneously.

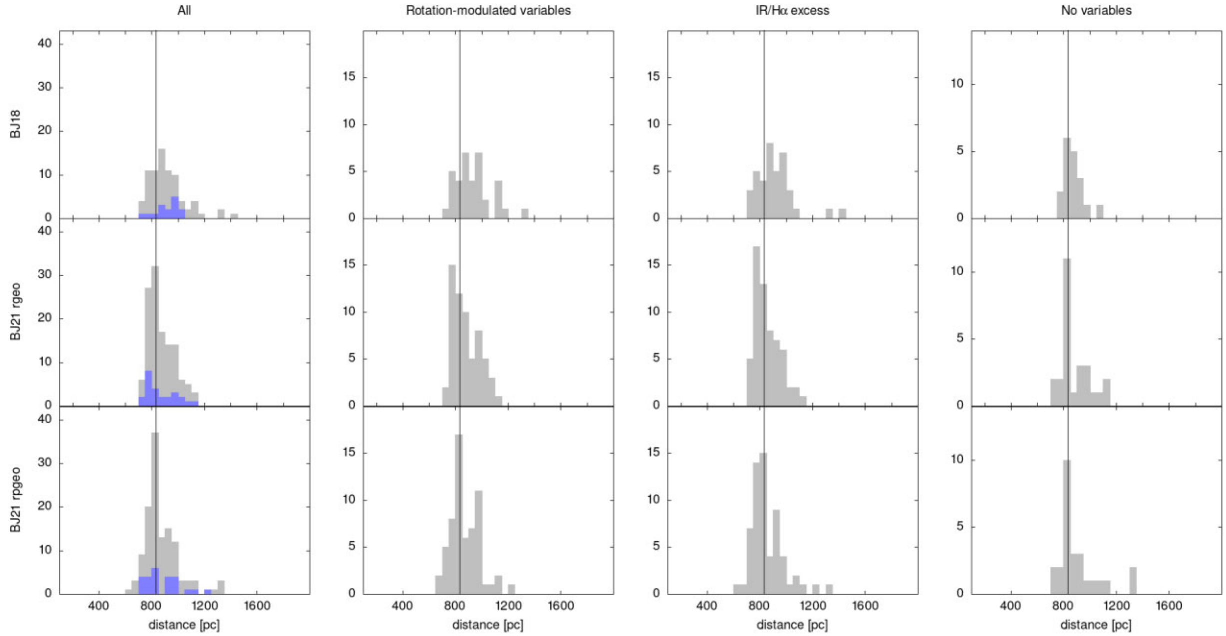

Figure E2. Distance histograms with BJ18 and BJ21 data with *GaiaFlag* = 1 sources and parallax errors less than 20 per cent. The vertical line is located at the $d = 825$ pc. The blue boxes are the sources with four membership flags simultaneously.

peak of the non-variable sources is only 50 pc away from the peak of the periodic ones.

APPENDIX F: TABLES

F1 Complete list of *Spitzer* data.

In Table F1, we presented the *Spitzer* sample mentioned in Section 2.2.3.

F2 Colour excess

In Table F3, we present the colour excess obtained for the study of A_V. We show the values of the different colours analysed E($g - r$), E($r - i$), E($z - y$), E($r - z$), E($i - z$), and E($i - y$). In Table F2, we present the A_λ/A_V coefficients obtained from the data in Wang & Chen (2019, table 3). Negative Av values are unphysical and the result of uncertainties; therefore, Av = 0.0 should be adopted in these cases.

F3 No candidates member

Some target with spectral type assigned could not be selected as members. Also, in Table F4, we show the stars with spectral type but no member indicators.

F4 Brown dwarf candidates

In Table F5, we presented the 11 spectroscopic BD stars. Moreover, in Table F6, we presented the photometrics BD candidates. However, this list should be taken with a lot of caution as it is likely to be contaminated by reddened low-mass stars.

Table F2. Coefficients obtained from the data in Wang & Chen (2019, table 3).

A_g/A_V	1.155	±0.009
A_r/A_V	0.843	±0.006
A_i/A_V	0.628	±0.004
A_z/A_V	0.487	±0.003
A_y/A_V	0.395	±0.003

Table F1. *Spitzer* data. The full table is in electronic table.

Id (1)	RA (2)	DEC (3)	[3.6] (4)	e[3.6] (5)	[4.5]	e[4.5]	[5.8]	e[5.8]	[8.0]	e[8.0]	Disc (6)	ref (7)	Spz_id (8)
6831.0	6:7:11.8152	−6:34:7.788	14.1327	5.90904	14.0449	5.39073	14.2479	3.65909	13.531	3.29265	1.0	1	J060711.83-063407.1
6832.0	6:7:46.608	−6:34:3.324	13.7221	6.17297	13.6658	5.68556	13.1706	4.67928	12.8134	4.0175	1.0	1	J060746.61-063402.9
6751.0	6:7:24.6336	−6:34:2.532	17.128	3.8929	16.7865	3.33417	999	999	14.5155	2.58389	1.0	1	J060724.42-063403.3
6706.0	6:7:23.3496	−6:34:0.516	11.8484	7.14405	11.7985	7.00212	11.7245	5.93091	11.7072	5.34458	0.0	1	J060723.36-063400.0
6818.0	6:8:7.1856	−6:33:59.796	13.2748	6.43814	13.2323	5.92525	13.117	4.91047	13.2122	3.70904	0.0	1	J060807.18-063359.3

(1) Internal identification object. (2) Right ascension and (3) declination in Equinox J2000. (4) *Spitzer* fluxes in magnitudes from four band [3.6], [4.5], [5.8], and [8.0] in 3.6 aperture and (5) error. (6) Disc presence (disc=1 and no disc=0). (7) Reference IRSA = 1, G9 = 2, and K12 = 3. (10) *Spitzer* id.

Table F3. Colour excess values for 124 sources. See columns notes in Table 4, the last 12 columns are the colour excess in E($g-r$) E($r-i$), E($z-y$), E($r-z$), E($i-z$), and E($i-y$) and its errors. The full table is in electronic table.

Id	RA	DEC	V_type	P(d)	Power	V_hs	Hα	SpT	Disc	ZamsFlag	GaiaFlag	Gaia_id	Spz_id	PS1_id	E($g-r$)	e_E($g-r$)	E($r-i$)	e_E($r-i$)	E($z-y$)	e_E($z-y$)	E($r-z$)	e_E($r-z$)	E($i-z$)	e_E($i-r$)	E($i-y$)	e_E($i-y$)
6346.0	6:7:31.716	−6:32:55.104	1.0	0.887	159	1	NH	M3	0	1	0	3018446360716527360	J060731.72-063254.7	100140918821792158	-2.9069	0.0614	1.787	0.1181	0.2015	0.0415	1.9979	0.1618	0.2109	0.0527	0.4124	0.0678
6273.0	6:7:32.8608	−6:32:40.38	1.0	6.337	312	1	Ha	M0	1	1	0	3018446360716735232	J060732.87-063239.9	100140918869497060	-2.7637	0.0571	1.8433	0.099	0.217	0.0355	2.109	0.1397	0.2657	0.0611	0.4827	0.0648
6260.0	6:7:22.7232	−6:32:39.516	0.0	0	55	1	NH	M3	0	1	1	3018447043615149056	J060722.73-063239.1	100140918447237354	-3.0902	0.0859	2.3088	0.1367	0.234	0.0402	2.5816	0.1706	0.2728	0.0585	0.5068	0.0763
6231.0	6:7:34.7328	−6:32:33.396	0.0	0	14	0	Ha	M6	1	1	0	3018447833889325952	J060734.74-063233.0	100140918947459385	-2.4972	0.2678	1.1182	0.3355	0.108	0.0575	1.2406	0.3885	0.1224	0.0858	0.2404	0.1245
6169.0	6:7:38.544	−6:32:20.472	3.0	1.263	143	1	NH	M6	1	1	1	3018447868248871680	J060738.55-063220.1	100150919106303676	-2.7172	0.145	1.1913	0.2084	-0.028	0.0513	1.1146	0.2664	-0.0767	0.0702	-0.0947	0.1133
6106.0	6:7:45.0384	−6:32:7.44	0.0	0	12	0	NH	M7	1	1	0	3018447902609799168	J060745.04-063207.1	100150919376728008	-1.4	0.3626	-0.557	0.342	0.0128	0.0663	-0.5996	0.4365	-0.0426	0.1259	-0.0198	0.2218
6007.0	6:7:30.4128	−6:31:45.912	1.0	6.337	436	0	Ha	M4	1	1	0	3018448662818095104	J060730.45-063145.2	100160918767995251	-3.1279	0.14	1.928	0.1979	0.2035	0.097	2.1431	0.2872	0.2151	0.1173	0.4186	0.1077
5998.0	6:7:30.1464	−6:31:43.536	0.0	0	81	0	Ha	M5	1	1	0	3018448662819492864	J060730.15-063143.2	100160918756285992	-2.5439	0.3004	1.3456	0.3112	0.2708	0.0523	1.5507	0.3509	0.2051	0.0621	0.3759	0.0926
5875.0	6:7:17.8368	−6:31:19.884	1.0	4.922	576	1	Ha	M0	1	1	1	3018459176898943488	J060717.84-063119.4	100170918243633888	-2.8139	0.0723	1.864	0.1078	0.1675	0.0444	2.1424	0.1461	0.2784	0.0613	0.4459	0.0761
5859.0	6:7:45.48	−6:31:12.828	0.0	0	22	0	Ha	M8	0	1	0	3018447936968356224	J060745.49-063112.6	100170919395126215	-1.53	0.2238	-0.539	0.2114	-0.1533	0.0818	-0.7903	0.2905	-0.2513	0.1081	-0.4046	0.1827

Table F4. Full table of objects with spectral type but not fulfilling the membership criteria. See columns notes in Table 4.

Id	RA	Dec.	V_type	P(d)	Power	V_hs	Hα	SpT	Disc	ZamsFlag	GaiaFlag
5376	06:07:23.38	−06:29:41.02	0	-	12	0	Ha-	nonM	-	0	0
5184	06:07:52.47	−06:28:48.36	0	-	51	0	Ha-	nonM	0	0	0
5121	06:08:29.11	−06:28:27.44	0	-	13	0	Ha-	nonM	-	0	0
5095	06:08:41.90	−06:28:17.40	0	-	28	0	Ha-	nonM	-	0	0
4941	06:08:02.83	−06:27:35.92	0	-	10	0	-	M3	-	0	0
4732	06:07:53.92	−06:26:34.44	0	-	16	0	NH	M3	-	0	0
4152	06:07:25.79	−06:24:06.37	0	-	8	0	Ha	M4	-	0	0
4100	06:07:16.51	−06:23:59.10	0	-	16	0	Ha-	nonM	-	0	0
3893	06:08:26.33	−06:23:16.11	0	-	17	0	Ha-	nonM	-	0	0
3624	06:08:34.71	−06:22:32.80	0	-	10	0	Ha-	nonM	-	0	0
3616	06:08:26.94	−06:22:31.87	0	-	13	0	Ha-	nonM	-	0	0
3117	06:08:42.77	−06:21:07.34	0	-	16	0	NH	M3	-	-	0
3090	06:08:31.20	−06:21:00.54	0	-	16	0	Ha-	nonM	-	0	0
2943	06:08:41.38	−06:20:25.80	0	-	17	0	Ha-	nonM	-	0	0
2625	06:08:36.18	−06:18:59.68	0	-	22	0	NH	nonM	-	0	0
2622	06:08:36.14	−06:18:59.18	0	-	15	0	NH	nonM	-	0	0
2543	06:08:44.48	−06:18:38.84	0	-	72	0	Ha-	nonM	-	-	0
2503	06:07:31.73	−06:18:34.20	0	-	10	0	Ha-	nonM	-	0	0
2317	06:08:14.75	−06:17:25.76	0	-	9	0	NH	M5	-	0	0
1927	06:08:13.61	−06:15:47.41	0	-	7	0	Ha-	nonM	-	0	0
1458	06:08:14.69	−06:14:02.72	0	-	26	0	Ha-	nonM	-	0	0
1365	06:08:16.14	−06:13:44.65	0	-	130	0	NH	M5	-	-	0
1145	06:08:13.95	−06:13:02.67	0	-	11	0	Ha-	nonM	-	0	0
1081	06:08:26.52	−06:12:49.42	0	-	16	0	Ha-	nonM	-	0	0
950	06:08:25.67	−06:12:30.67	0	-	10	0	Ha	M3	-	0	0

Table F5. Spectroscopic BD table. See columns notes in Table 4.

Id	RA	DEC	V_type	P(d)	Power	V_hs	Hα	SpT	Disc	ZamsFlag	GaiaFlag	Gaia_id	Spz_id	PS1_id
6106	06:07:45.03	−06:32:07.44	0	-	12	0	NH	M7	1	1	0	3018447902609799168	J060745.04-063207.1	100150919376728008
5859	06:07:45.48	−06:31:12.82	0	-	22	0	Ha	M8	0	1	0	3018447936968356224	J060745.49-063112.6	100170919395126215
4667	06:08:18.92	−06:26:07.58	0	-	46	0	Ha	M7	1	1	0	3019950179090847744	J060818.92-062607.3	100270920788647948
4559	06:08:20.13	−06:25:37.23	4	12.597	277	0	Ha	M8	1	1	1	3019950179090848128	J060820.13-062537.0	100280920838988066
4319	06:07:52.89	−06:24:38.44	0	-	31	0	Ha	M9	1	1	0	3019951008020170880	J060752.91-062437.9	100300919704297661
3501	06:07:54.76	−06:22:16.46	0	-	30	0	Ha	M9	1	1	0	3019963270150782720	-	100350919782144985
2915	06:07:39.24	−06:20:27.52	0	-	97	0	Ha	M9	1	1	0	3019963957346220288	J060739.41-062025.3	100390919135431294
2668	06:07:42.57	−06:19:18.12	0	-	10	0	NH	M8	1	1	0	-	J060742.57-061917.9	100410919273694448
2044	06:07:28.86	−06:16:20.20	0	-	12	0	Ha	M7	1	1	0	-	J060728.86-061619.9	100470918702823749
1692	06:07:52.62	−06:14:57.62	0	-	27	0	Ha	M7	1	1	1	3019966435541404672	J060752.61-061457.4	100500919692871279
1531	06:07:49.99	−06:14:18.13	3	4.332	233	0	Ha	M7	1	1	0	3019969454903697792	J060749.99-061417.8	100510919583154445

Table F6. BD candidates. The full table is in electronic table. See columns notes in Table 4.

Id	RA	Dec.	V_type	P(d)	Power	V_hs	Hα	SpT	Disc	ZamsFlag	GaiaFlag	GaiaFlag Gaia_id	Spz_id	PS1_id
6429	06:07:49.86	−06:33:07.92	4	25	176	0	-	-	-	1	0	3018447627731892736	J060749.86-063307.5	100130919577597860
5075	06:07:47.88	−06:28:16.68	0	-	10	0	-	-	1	1	0	3018449345717877120	J060747.88-062816.4	100230919495224918
4487	06:08:05.23	−06:25:20.92	1	4.174	125	0	-	-	1	1	0	3019951076738096128	J060805.23-062520.6	100290920218123505
4308	06:07:45.61	−06:24:35.20	0	-	16	0	-	-	1	1	0	3019962651675489024	-	100300919400888732
4292	06:07:48.03	−06:24:30.85	1	4.712	482	1	-	-	1	1	0	3019962655971478144	J060748.02-062430.6	100310919501410198
3898	06:07:51.44	−06:23:21.40	0	-	69	0	-	-	1	1	0	-	J060751.44-062321.0	100330919643433304
3739	06:07:47.69	−06:22:55.48	2	5.986	154	0	-	-	-	1	0	3019962862128625024	-	100340919487391974
3708	06:07:39.99	−06:22:52.60	0	-	10	0	-	-	1	1	0	3019962995272608640	J060739.99-062252.2	100340919166712936
3648	06:08:22.14	−06:22:38.31	1	1.207	536	1	-	-	1	1	0	3019952000156332800	J060822.14-062238.1	100340920922917700
2277	06:07:39.92	−06:17:19.75	0	-	96	0	-	-	1	1	1	3019967702557748224	J060739.91-061719.5	100450919163533901
1694	06:08:11.19	−06:14:56.25	0	-	51	0	-	-	1	1	1	3019966603045411712	J060811.19-061455.7	100500920466361735

This paper has been typeset from a TEX/LATEX file prepared by the author.